The Astrophysical Journal, 691:1540–1559, 2009 February 1 doi:10.1088/0004-637X/691/2/1540

A NEW APPROACH TO ANALYZING SOLAR CORONAL SPECTRA AND UPDATED COLLISIONAL IONIZATION EQUILIBRIUM CALCULATIONS. II. UPDATED IONIZATION RATE COEFFICIENTS

P. Bryans[1,3], E. Landi[2], and D. W. Savin[1]
[1] Columbia Astrophysics Laboratory, Columbia University, New York, NY 10027, USA
[2] US Naval Research Laboratory, Space Science Division, 4555 Overlook Avenue, SW, Code 7600A, Washington, DC 20375, USA
Received 2008 May 21; accepted 2008 October 12; published 2009 February 5

ABSTRACT

We have re-analyzed Solar Ultraviolet Measurement of Emitted Radiation (SUMER) observations of a parcel of coronal gas using new collisional ionization equilibrium (CIE) calculations. These improved CIE fractional abundances were calculated using state-of-the-art electron–ion recombination data for K-shell, L-shell, Na-like, and Mg-like ions of all elements from H through Zn and, additionally, Al- through Ar-like ions of Fe. They also incorporate the latest recommended electron impact ionization data for all ions of H through Zn. Improved CIE calculations based on these recombination and ionization data are presented here. We have also developed a new systematic method for determining the average emission measure (EM) and electron temperature (T_e) of an isothermal plasma. With our new CIE data and a new approach for determining average EM and T_e, we have re-analyzed SUMER observations of the solar corona. We have compared our results with those of previous studies and found some significant differences for the derived EM and T_e. We have also calculated the enhancement of coronal elemental abundances compared to their photospheric abundances, using the SUMER observations themselves to determine the abundance enhancement factor for each of the emitting elements. Our observationally derived first ionization potential factors are in reasonable agreement with the theoretical model of Laming.

Key words: atomic data – atomic processes – plasmas – Sun: corona – Sun: UV radiation

Online-only material: figure sets, machine-readable table

1. INTRODUCTION

Investigating the dynamics of the solar corona is crucial if one is to understand fundamental solar and heliospheric physics. The corona also greatly influences the Sun–Earth interaction, as it is from here that the solar wind originates. Explosive events in the corona can deposit up to 2×10^{16} g of ionized particles into the solar wind (Hundhausen 1993). These can have a profound effect on the Earth's magnetosphere and ionosphere. Hence the investigation of the corona is of obvious importance.

Over the years there has been a significant amount of research invested in developing our understanding of the corona (reviewed by Aschwanden 2004 and Foukal 2004). However, gaps remain in our understanding of some of the most fundamental processes taking place in the corona. For example, the so-called coronal heating problem remains unsolved (Gudiksen & Nordlund 2005; Klimchuk 2006) and we are still unable to explain the onset processes that cause solar flares and coronal mass ejections (Forbes 2000; Priest & Forbes 2002).

One of the most powerful tools for understanding the properties of the solar corona is spectroscopy (Tandberg-Hanssen & Emslie 1988; Foukal 2004). Analyzing the spectral emission of the corona can give the temperature and density of the plasma, as well as information on the complex plasma structures common in this region of the Sun's atmosphere. One common approach to this end is to calculate the emission measure (EM) of the gas (e.g., Raymond & Doyle 1981).

The EM technique is particularly useful for studying the properties of the upper solar atmosphere. In this region, conditions are such that the plasma can often be described as low density and in steady state and the emitting region as constant in density and temperature. These relatively simple conditions allow one to neglect density effects and to assume all emission is from an isothermal plasma. For example, Landi et al. (2002) compared off-disk spectral observations of the solar corona with predictions from the CHIANTI version 3 atomic database (Dere et al. 1997, 2001). Landi et al. (2002) calculated the EM of the plasma based on the observed intensities using the atomic data assembled together in CHIANTI. From this, they also infer the electron temperature (T_e) of the emitting plasma. However, the power of this spectroscopic diagnostic can be limited by our understanding of the underlying atomic physics that produce the observed spectrum.

Reliable EM calculations require accurate fractional abundances for the ionization stages of the elements present in the plasma. For a plasma in collisional ionization equilibrium (CIE; sometimes also called coronal equilibrium), the atomic data needed for such a spectral analysis includes rate coefficients for electron–ion recombination and electron impact ionization (EII). These data directly affect the calculated ionic fractional abundances of the gas. The fractional abundances, in turn, are used to determine the EM. Hence the reliability of the CIE calculations is critical.

The recommended CIE calculations at the time of the work by Landi et al. (2002) were those of Mazzotta et al. (1998). Recently, however, state-of-the-art electron–ion recombination data have been published for K-shell, L-shell, and Na-like ions of all elements from H through Zn (Badnell et al. 2003; Badnell 2006a, 2006b, 2006c; Gu 2003a, 2003b, 2004). Based on these new recombination data, a significant update of the recommended CIE fractional abundances was published recently by Bryans et al. (2006, Paper I in this series). Since then additional recombination data have been published for Mg-like ions of H through Zn (Altun et al. 2007) and Al- through Ar-like ions of Fe (Badnell 2006d, 2006e). EII data have also

[3] Present Address: US Naval Research Laboratory, Space Science Division, 4555 Overlook Avenue, SW, Code 7670, Washington, DC 20375, USA.

been updated recently by Suno & Kato (2006), Dere (2007), and Mattioli et al. (2007). Of these three, the recommended EII data of Dere (2007), which we adopt, provide the only complete available set of rate coefficients for all ions of H through Zn. Here we have updated the results of Bryans et al. (2006) using these new recombination and ionization data. One of the motivations behind this paper is to investigate the effects of the recent improvements in CIE calculations on solar observations.

Since the Landi et al. (2002) paper there have been other improved atomic data (e.g., the improvement of the model for N-like ions). These have been made available in a more recent CHIANTI release—version 5.2 (Landi et al. 2006). It is this version we use here.

We also investigate here the observed relative elemental abundances and the first ionization potential (FIP) effect. The FIP effect is the discrepancy between the coronal and photospheric elemental abundances, possibly explained by the pondermotive force induced by the propagation of Alfvén waves through the chromosphere (Laming 2004, 2009). Elements with a FIP below $\sim$ 10 eV appear to have a coronal abundance that is enhanced by a factor of a few over their photospheric abundance (see, e.g., the review by Feldman & Laming 2000). Often, the FIP effect is accounted for by multiplying the abundance of the low-FIP elements by a single scaling factor (such as 3.5, as was done in Landi et al. 2002). In the present work, we investigate the reliability of this approach by quantifying the FIP effect based on the observations themselves. We determine the EM from the high-FIP element Ar and then scale the elemental abundances of the moderate- and low-FIP elements so that their derived EMs match that of Ar. We compare our derived abundances with those of a previous analysis of the same observation (Feldman et al. 1998) as well as with theoretical predictions (Laming 2009).

An important aspect of this paper is the development of a sound mathematical method of determining the average EM and T_e of an isothermal plasma. Previous studies have done this in a less rigorous manner. Landi et al. (2002), for example, evaluate plots of EM versus T_e curves and give a "by-eye" estimate of the average value of the EM and T_e and their associated errors. This method allows human bias to become important when deciding which curve crossings to include in the selection. In addition, it is unclear to what this "average" actually corresponds mathematically. The fact that the analysis is performed on graphs with logarithmic axes suggests that by-eye average is closer to the geometric mean than the arithmetic mean. Finally, no account is taken of the reliability of the atomic data used to calculate fractional abundances. Bryans et al. (2006) showed that CIE results are unreliable at temperatures where the ionic fractional abundances are less than 1%. Previous studies have failed to account for this when using the CIE data in the EM analysis.

Taking the above four paragraphs into account, we have reanalyzed the observations of Landi et al. (2002). The rest of this paper is organized as follows. In Section 2 we give a description of the observing sequence, the observed lines, and their categorizations by Landi et al. (2002). Section 3 defines the EM and explains the method we use to determine the plasma temperature from the observed line intensities. In Section 4 we review the recent developments in the understanding of dielectronic and radiative recombinations (DR and RR) and EII, and the subsequent improvement in CIE calculations. We also present updated tables of these CIE calculations, which supersede those of Bryans et al. (2006). In Section 5 we describe our new approach for determining the EM and temperature of an isothermal plasma based on the observed spectral line intensities. Section 6 discusses our method of determining the elemental abundance enhancement factors due to the FIP effect. In Section 7 we present the results of our EM calculations for each of the categorizations introduced by Landi et al. (2002). Section 8 discusses the consequences of these results, in particular highlighting discrepancies between the results of this paper and those of Landi et al. (2002). In Section 9 we propose future observations needed to address some of the remaining issues raised by our results here. Concluding remarks are given in Section 10.

2. OBSERVATIONS

The spectrum analyzed by Landi et al. (2002), and revisited here, was detected using the Solar Ultraviolet Measurement of Emitted Radiation Spectrometer (SUMER; Wilhelm et al. 1995) onboard the *Solar and Heliospheric Observatory* (*SOHO*). The observation spans over 5 hr, from 21:16 UT on 1996 November 21 to 02:28 UT on 1996 November 22, and was collected in 61 spectral sections. The observing slit imaged at a height h of $1.03\,R_\odot \lesssim h \lesssim 1.3\,R_\odot$ above the western limb. The resulting spectrum covers the entire SUMER spectral range of 660–1500 Å. Landi et al. (2002) give a full description of the observation sequence and data reduction.

Table 1 lists the coronal lines identified in the spectrum and their corresponding transitions (reproduced from Landi et al. 2002). Known typos in the line assignment labels of Landi et al. (2002) have been corrected; these do not affect their reported results. Landi et al. estimate uncertainties on the extracted line intensities of 25%–30%. Twelve of the emission lines observed in this run are omitted from the table here due to their being blended with other emission lines or having uncertain intensities. The remaining spectral lines are split into three distinct groups, labeled in the first column of Table 1 as

I. Forbidden transitions within the ground configuration:
   - Ia. Non-N-like transitions.
   - Ib. N-like transitions.

II. Transitions between the ground and the first excited configuration:
   - IIa. Allowed $2s$–$2p$ transitions in the Li-like isoelectronic sequence and allowed $3s$–$3p$ transitions in the Na-like isoelectronic sequence.
   - IIb. Intercombination transitions in the Be-, B-, C-, and Mg-like isoelectronic sequences.

III. Transitions between the first and second excited configuration.

Within each group and subgroup we have derived the average T_e and EM. Categorizing the transitions in this way helps us to better identify any trends in the EM with respect to the transition type. Group I transitions have been further divided into non-N-like and N-like transitions. This separation was originally proposed by Landi et al. (2002) due to the poor agreement they found for the T_e derived within each of these transition types. This is discussed further in Sections 6 and 8. The subdivision of transition Group II is to allow us to investigate a longstanding discrepancy between EMs derived using Li- and Na-like ions and those derived using other isoelectronic sequences (e.g., Dupree 1972; Feldman et al. 1998; Landi et al. 2002). We also discuss this further in Sections 6 and 8.

Table 1
Emission Lines and Intensities Used in the Present Study

Group	Ion	Sequence	Wavelength (Å)	Transition	Intensity (ergs cm^{-2} s^{-1} sr^{-1})
IIa	N V	Li	1238.82	$2s\ ^2S_{1/2}–2p\ ^2P_{3/2}$	2.520
IIa	N V	Li	1242.80	$2s\ ^2S_{1/2}–2p\ ^2P_{1/2}$	1.420
IIa	O VI	Li	1031.91	$2s\ ^2S_{1/2}–2p\ ^2P_{3/2}$	63.000
IIa	O VI	Li	1037.62	$2s\ ^2S_{1/2}–2p\ ^2P_{1/2}$	28.500
IIa	Ne VIII	Li	770.41	$2s\ ^2S_{1/2}–2p\ ^2P_{3/2}$	30.700
IIa	Ne VIII	Li	780.32	$2s\ ^2S_{1/2}–2p\ ^2P_{1/2}$	14.200
IIb	Ne VII	Be	895.17	$2s^2\ ^1S_0–2s2p\ ^3P_1$	0.132
III	Ne VII	Be	973.33	$2s2p\ ^1P_1–2p^2\ ^1D_2$	0.070
IIa	Na IX	Li	681.72	$2s\ ^2S_{1/2}–2p\ ^2P_{3/2}$	4.515
IIa	Na IX	Li	694.13	$2s\ ^2S_{1/2}–2p\ ^2P_{1/2}$	2.600
IIb	Na VIII	Be	789.78	$2s^2\ ^1S_0–2s2p\ ^3P_1$	0.074
III	Na VIII	Be	847.91	$2s2p\ ^1P_1–2p^2\ ^1D_2$	0.058
IIa	Mg X	Li	609.79	$2s\ ^2S_{1/2}–2p\ ^2P_{3/2}$	153.000
IIa	Mg X	Li	624.94	$2s\ ^2S_{1/2}–2p\ ^2P_{1/2}$	91.700
IIb	Mg IX	Be	693.98	$2s^2\ ^1S_0–2s2p\ ^3P_2$	0.898
IIb	Mg IX	Be	706.06	$2s^2\ ^1S_0–2s2p\ ^3P_1$	8.160
III	Mg IX	Be	749.55	$2s2p\ ^1P_1–2p^2\ ^1D_2$	1.490
IIb	Mg VIII	B	762.66	$2s^22p\ ^2P_{1/2}–2s2p^2\ ^4P_{3/2}$	0.047
IIb	Mg VIII	B	769.38	$2s^22p\ ^2P_{1/2}–2s2p^2\ ^4P_{1/2}$	0.152
IIb	Mg VIII	B	772.28	$2s^22p\ ^2P_{3/2}–2s2p^2\ ^4P_{5/2}$	0.670
IIb	Mg VIII	B	782.36	$2s^22p\ ^2P_{3/2}–2s2p^2\ ^4P_{3/2}$	0.357
IIb	Mg VIII	B	789.43	$2s^22p\ ^2P_{3/2}–2s2p^2\ ^4P_{1/2}$	0.099
IIb	Mg VII	C	868.11	$2s^22p^2\ ^3P_2–2s2p^3\ ^5S_2$	0.048
IIa	Al XI	Li	549.98	$2s\ ^2S_{1/2}–2p\ ^2P_{3/2}$	7.820
IIa	Al XI	Li	568.18	$2s\ ^2S_{1/2}–2p\ ^2P_{1/2}$	5.050
IIb	Al X	Be	637.76	$2s^2\ ^1S_0–2s2p\ ^3P_1$	2.070
III	Al X	Be	670.01	$2s2p\ ^1P_1–2p^2\ ^1D_2$	0.265
IIb	Al IX	B	688.25	$2s^22p\ ^2P_{1/2}–2s2p^2\ ^4P_{1/2}$	0.076
IIb	Al IX	B	691.54	$2s^22p\ ^2P_{3/2}–2s2p^2\ ^4P_{5/2}$	0.441
IIb	Al IX	B	703.65	$2s^22p\ ^2P_{3/2}–2s2p^2\ ^4P_{3/2}$	0.205
IIb	Al IX	B	712.23	$2s^22p\ ^2P_{3/2}–2s2p^2\ ^4P_{1/2}$	0.058
IIb	Al VIII	C	756.70	$2s^22p^2\ ^3P_1–2s2p^3\ ^5S_2$	0.036
IIb	Al VIII	C	772.54	$2s^22p^2\ ^3P_2–2s2p^3\ ^5S_2$	0.055
Ib	Al VII	N	1053.84	$2s^22p^3\ ^4S_{3/2}–2s^22p^3\ ^2P_{3/2}$	0.017
Ia	Al VIII	C	1057.85	$2s^22p^2\ ^3P_1–2s^22p^2\ ^1S_0$	0.036
IIa	Si XII	Li	499.40	$2s\ ^2S_{1/2}–2p\ ^2P_{3/2}$	19.200
IIa	Si XII	Li	520.67	$2s\ ^2S_{1/2}–2p\ ^2P_{1/2}$	9.160
III	Si X	B	551.18	$2s2p^2\ ^2P_{3/2}–2p^3\ ^2D_{5/2}$	0.200
IIb	Si XI	Be	564.02	$2s^2\ ^1S_0–2s2p\ ^3P_2$	1.110
IIb	Si XI	Be	580.91	$2s^2\ ^1S_0–2s2p\ ^3P_1$	16.000
III	Si XI	Be	604.15	$2s2p\ ^1P_1–2p^2\ ^1D_2$	1.840
IIb	Si X	B	611.60	$2s^22p\ ^2P_{1/2}–2s2p^2\ ^4P_{3/2}$	0.553
IIb	Si X	B	624.70	$2s^22p\ ^2P_{3/2}–2s2p^2\ ^4P_{5/2}$	6.970
IIb	Si X	B	638.94	$2s^22p\ ^2P_{3/2}–2s2p^2\ ^4P_{3/2}$	5.210
IIb	Si X	B	649.19	$2s^22p\ ^2P_{3/2}–2s2p^2\ ^4P_{1/2}$	1.510
IIb	Si IX	C	676.50	$2s^22p^2\ ^3P_1–2s2p^3\ ^5S_2$	1.560
IIb	Si IX	C	694.70	$2s^22p^2\ ^3P_2–2s2p^3\ ^5S_2$	3.550
Ib	Si VIII	N	944.38	$2s^22p^3\ ^4S_{3/2}–2s^22p^3\ ^2P_{3/2}$	2.030
Ib	Si VIII	N	949.22	$2s^22p^3\ ^4S_{3/2}–2s^22p^3\ ^2P_{1/2}$	0.870
Ia	Si IX	C	950.14	$2s^22p^2\ ^3P_1–2s^22p^2\ ^1S_0$	1.920
Ia	Si VII	O	1049.22	$2s^22p^4\ ^3P_1–2s^22p^4\ ^1S_0$	0.045
Ib	Si VIII	N	1440.49	$2s^22p^3\ ^4S_{3/2}–2s^22p^3\ ^2D_{5/2}$	0.176
Ib	Si VIII	N	1445.76	$2s^22p^3\ ^4S_{3/2}–2s^22p^3\ ^2D_{3/2}$	2.090
IIb	S XI	C	552.12	$2s^22p^2\ ^3P_1–2s2p^3\ ^5S_2$	0.190
IIb	S XI	C	574.89	$2s^22p^2\ ^3P_2–2s2p^3\ ^5S_2$	0.470
Ib	S X	N	776.25	$2s^22p^3\ ^4S_{3/2}–2s^22p^3\ ^2P_{3/2}$	1.910
Ia	S XI	C	782.96	$2s^22p^2\ ^3P_1–2s^22p^2\ ^1S_0$	0.4005
Ib	S X	N	787.56	$2s^22p^3\ ^4S_{3/2}–2s^22p^3\ ^2P_{1/2}$	0.946
Ia	S IX	O	871.73	$2s^22p^4\ ^3P_1–2s^22p^4\ ^1S_0$	0.440
Ib	S X	N	1196.26	$2s^22p^3\ ^4S_{3/2}–2s^22p^3\ ^2D_{5/2}$	1.590
Ib	S X	N	1212.93	$2s^22p^3\ ^4S_{3/2}–2s^22p^3\ ^2D_{3/2}$	3.410
IIa	Ar VIII	Na	700.25	$3s\ ^2S_{1/2}–3p\ ^2P_{3/2}$	0.635
IIa	Ar VIII	Na	713.81	$3s\ ^2S_{1/2}–3p\ ^2P_{1/2}$	0.310
Ib	Ar XII	N	1018.89	$2s^22p^3\ ^4S_{3/2}–2s^22p^3\ ^2D_{5/2}$	0.274
Ib	Ar XII	N	1054.57	$2s^22p^3\ ^4S_{3/2}–2s^22p^3\ ^2D_{3/2}$	0.056

Table 1
(Continued)

Group	Ion	Sequence	Wavelength (Å)	Transition	Intensity (ergs cm^{-2} s^{-1} sr^{-1})
Ia	Ar XI	O	1392.11	$2s^2 2p^4\ ^3P_2$–$2s^2 2p^4\ ^1D_2$	0.134
IIa	K IX	Na	636.29	$3s\ ^2S_{1/2}$–$3p\ ^2P_{1/2}$	0.133
IIa	Ca X	Na	557.76	$3s\ ^2S_{1/2}$–$3p\ ^2P_{3/2}$	8.000
IIa	Ca X	Na	574.00	$3s\ ^2S_{1/2}$–$3p\ ^2P_{1/2}$	4.880
IIb	Ca IX	Mg	691.41	$3s^2\ ^1S_0$–$3s3p\ ^3P_1$	0.109
III	Ca IX	Mg	821.23	$3s3p\ ^1P_1$–$3p^2\ ^1D_2$	0.048
Ia	Fe XII	P	1242.00	$3s^2 3p^3\ ^4S_{3/2}$–$3s^2 3p^3\ ^2P_{3/2}$	11.840
Ia	Fe XII	P	1349.36	$3s^2 3p^3\ ^4S_{3/2}$–$3s^2 3p^3\ ^2P_{1/2}$	5.353
Ia	Fe XI	S	1467.06	$3s^2 3p^4\ ^3P_1$–$3s^2 3p^4\ ^1S_0$	3.390

Notes. We list here all the emission lines of the SUMER 1996 November 21 21:16 UT to 1996 November 22 02:28 UT observation that are used in the analysis here. This table is reproduced from Landi et al. (2002) with known transition assignment errors corrected. Lines that are blended or have uncertain intensities have also been omitted.

3. METHOD OF CALCULATING TEMPERATURE AND EM

The intensity of an observed spectral line due to a transition from level j to level i in element X of ionization state $+m$ can be written as

$$I_{ji} = \frac{1}{4\pi d^2}\int_V G_{ji}(T_e, n_e) n_e^2\, dV, \tag{1}$$

where n_e is the electron density, V is the emitting volume along the line of sight, and d is the distance to the source. $G_{ji}(T_e, n_e)$ is the contribution function, which is defined as

$$G_{ji}(T_e, n_e) = \frac{n_j(\mathrm{X}^{+m})}{n(\mathrm{X}^{+m})}\frac{n(\mathrm{X}^{+m})}{n(\mathrm{X})}\frac{n(\mathrm{X})}{n(\mathrm{H})}\frac{n(\mathrm{H})}{n_e}\frac{A_{ji}}{n_e}, \tag{2}$$

where $n_j(\mathrm{X}^{+m})/n(\mathrm{X}^{+m})$ is the population of the upper level j relative to all levels in X^{+m}, $n(\mathrm{X}^{+m})/n(\mathrm{X})$ is the fractional abundance of the ionization stage $+m$ relative to the sum of all ionization stages of X, $n(\mathrm{X})/n(\mathrm{H})$ is the abundance of element X relative to hydrogen, and $n(\mathrm{H})/n_e$ is the abundance of hydrogen relative to the electron density. A_{ji} is the spontaneous emission coefficient for the transition.

For the observation analyzed here, the emitting plasma was found to be isothermal by Feldman et al. (1998) and Landi et al. (2002). For the moment we assume this to be correct but we revisit the validity of the isothermal assumption in Section 8.4. One can also make the assumption that the region emitting the observed line intensities is at a constant density. While the line of sight of the observation covers plasma where densities vary by orders of magnitude, the emission is dominated by a region with a small range of densities around the peak density. Only those emission lines that have a strong density sensitivity in this range will be affected by the density gradient (Lang et al. 1990). Feldman et al. (1999) inferred a density of 1.8×10^8 cm^{-3} for this observation. A density-dependent study of the 74 lines observed here is beyond the scope of our paper. Here we use the inferred density of Feldman et al. (1999) in our analysis.

If we now assume that all the emission comes from the same parcel of gas of nearly constant temperature, T_c, and density, we can approximate

$$I_{ji} = \frac{G_{ji}(T_c, n_e)}{4\pi d^2}\mathrm{EM}, \tag{3}$$

where the EM is defined as

$$\mathrm{EM} = \int n_e^2\, dV \tag{4}$$

and can be evaluated from the observed line intensity as

$$\mathrm{EM} = 4\pi d^2 \frac{I_{ji}}{G_{ji}(T_c, n_e)}. \tag{5}$$

This has the same value for all transitions if the constant temperature and density assumption is correct, which we label EM_c. Thus, from the observed line intensities, I_{ji}, and using accurate data for $G_{ji}(T_e, n_e)$, one can calculate the EM and T_e of the emitting region. This is done by plotting the EM against T_e. The resulting curves for each observed line should intersect at a common point yielding $[T_c, \mathrm{EM}_c]$. But this depends on the assumption of constant temperature and density being correct and on the accuracy of the underlying atomic data. Here, one of the issues we are investigating is the effect on solar coronal observations of the newly calculated fractional abundances

$$f^m = \frac{n(\mathrm{X}^{+m})}{n(\mathrm{X})}. \tag{6}$$

The units used throughout this paper for EM and T_e are cm^{-3} and K, respectively. For ease of reading, we typically drop these units below.

4. IMPROVED CIE CALCULATIONS

The plasma conditions of the solar upper atmosphere are often described as being optically thin, low density, dust free, and in steady state or quasi-steady state. Under these conditions the effects of any radiation field can be ignored, three-body collisions are unimportant, and the ionization balance of the gas is time-independent. This is commonly called CIE or coronal equilibrium. These conditions are not always the case in the solar upper atmosphere in the event of impulsive heating events but, given the inactivity and low density of the plasma analyzed here, they sufficiently describe the observed conditions. For a thorough discussion of plasma conditions where one must treat the timescales and density effects more carefully, we direct the reader to Summers et al. (2006).

In CIE, recombination is due primarily to DR and RR. At the temperature of peak formation in CIE, DR dominates over

RR for most ions. Ionization is primarily a result of EII. At temperatures low enough for both atoms and ions to exist, charge transfer (CT) can be both an important recombination and ionization process (Arnaud & Rothenflug 1985; Kingdon & Ferland 1996). CT is not expected to be important at solar coronal temperatures and is not included in the work of Mazzotta et al. (1998), Bryans et al. (2006), or this paper. Considering all the ions and levels that need to be taken into account, it is clear that vast quantities of data are needed. Generating them to the accuracy required pushes atomic theoretical and experimental methods to the edge of what is currently achievable and often beyond. For this reason, the CIE data used by the solar physics and astrophysics communities have gone through numerous updates over the years as more reliable atomic data have become available.

4.1. Recombination Rate Coefficients

The DR and RR rate coefficients used to determine the CIE fractional abundances utilized by Landi et al. (2002) were those recommended by Mazzotta et al. (1998). However, there has been a significant improvement in the recombination rate coefficients since then. Badnell et al. (2003) and Badnell (2006a, 2006b, 2006c) have calculated DR and RR rate coefficients for all ionization stages from bare through Na-like for all elements from H through Zn and Gu (2003a, 2003b, 2004) for a subset of these elements. The methods of Badnell and Gu are of comparable sophistication and their DR results for a given ion agree with one another typically to better than 35% at the electron temperatures where the CIE fractional abundance of that ion is $\geqslant 1\%$. The RR rate coefficients are in even better agreement, typically within 10% over this temperature range. These differences for the DR and RR rate coefficients do not appear to be systematic in any way (Bryans et al. 2006). For both DR and RR outside this temperature range, agreement between these two state-of-the-art theories can become significantly worse. The DR calculations have also been compared to experimental measurements, where they exist, and found to be in agreement to within 35% in the temperature range where the ion forms in CIE. For a fuller discussion of the agreement between recent theories and the agreement between theory and experiment, we direct the reader to Bryans et al. (2006).

4.2. EII Rate Coefficients

There have also been recent attempts to improve the state of the EII rate coefficients used in CIE calculations. The most complete of these studies is that of Dere (2007), who produced recommended rate coefficients for all ionization stages of the elements H through Zn. These data are based on a combination of laboratory experiments and theoretical calculations. In addition, there have been works by Suno & Kato (2006) and Mattioli et al. (2007) that also address the issue of updating the EII database. These works are less complete than that of Dere (2007). Suno & Kato (2006) provides EII cross sections for all ionization stages of C. Mattioli et al. (2007) provide EII cross sections for all ionization stages of H through O plus Ne and a selection of other ions up to Ge.

Between these recent compilations there remain sizable differences in the EII rate coefficients for certain elements, often in the temperature range where an ion forms in CIE. For the ions important to the present work, differences between recent recommended rate coefficients of up to 50% are seen. Larger differences, of up to a factor of ~ 4, are found for other ions not observed in this SUMER observation. In short, we do not see

Table 2
CIE Fractional Abundances (Iron)

log(T)	Fe^{0+}	Fe^{1+}
4.00	0.901	0.058
4.10	1.416	0.020
4.20	1.932	0.085
4.30	2.825	0.587
4.40	3.877	1.291
4.50	4.692	1.794
4.60	5.580	2.399
4.70	6.502	3.061
4.80	7.319	3.639
4.90	8.194	4.290
5.00	9.169	5.056
5.10	10.239	5.927
5.20	11.367	6.865
5.30	12.564	7.879
5.40	13.890	9.028
5.50	15.000	10.326
5.60	15.000	11.714
5.70	15.000	13.149
5.80	15.000	14.619
5.90	15.000	15.000
6.00	15.000	15.000
6.10	15.000	15.000
6.20	15.000	15.000
6.30	15.000	15.000
6.40	15.000	15.000
6.50	15.000	15.000
6.60	15.000	15.000
6.70	15.000	15.000
6.80	15.000	15.000
6.90	15.000	15.000
7.00	15.000	15.000
7.10	15.000	15.000
7.20	15.000	15.000
7.30	15.000	15.000
7.40	15.000	15.000
7.50	15.000	15.000
7.60	15.000	15.000
7.70	15.000	15.000
7.80	15.000	15.000
7.90	15.000	15.000
8.00	15.000	15.000
8.10	15.000	15.000
8.20	15.000	15.000
8.30	15.000	15.000
8.40	15.000	15.000
8.50	15.000	15.000
8.60	15.000	15.000
8.70	15.000	15.000
8.80	15.000	15.000
8.90	15.000	15.000
9.00	15.000	15.000

Notes. Calculated $-\log_{10}$ of the fractional abundance for ionization stages of iron. We only show the first two ionization stages here. All ionization stages are available in the online version of the table. We use the DR rate coefficients of Badnell (2006b) and the RR rate coefficients of Badnell (2006c) where they exist and use the DR and RR rate coefficients of Mazzotta et al. (1998) for ions not calculated by Badnell (2006b, 2006c). The EII rate coefficients of Dere (2007) are used. Fractional abundances are cut off at 10^{-15}. For ease of machine readability, values less than 10^{-15} are given $-\log_{10}$ values of 15.

(This table is available in its entirety in a machine-readable form in the online journal. A portion is shown here for guidance regarding its form and content.)

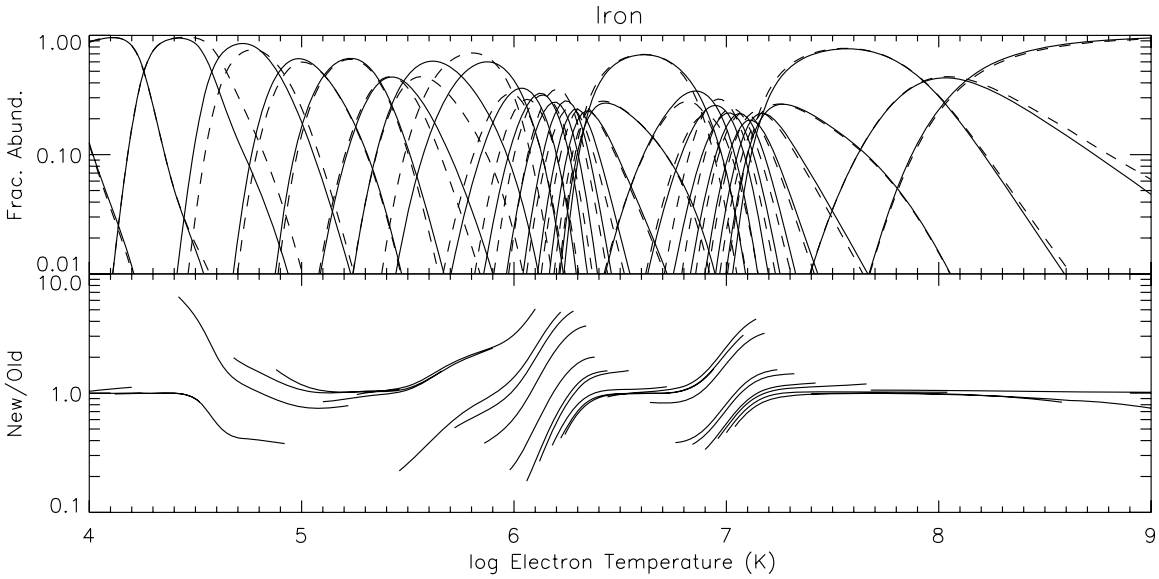

Figure 1. Ionization fractional abundance vs. T_e for all ionization stages of Fe. The upper graph shows our results (solid curves) and the abundances calculated by Mazzotta et al. (1998; dashed curves). The lower graph shows the ratio of the calculated abundances. Comparison is made only for fractional abundances greater than 10^{-2}. We label our results as "New" and those of Mazzotta et al. (1998) as "Old."

(An extended version of this figure set is available in the online journal.)

the uniform agreement between recommended sets of EII data as we do for the state-of-the-art DR and RR calculations.

Despite these outstanding issues regarding the accuracy of the various EII databases, we have used the compilation of Dere (2007) to calculate fractional CIE abundances. Of the recent EII compilations, the Dere database offers the most complete selection of rate coefficients. However, given the large differences between the Dere (2007) and Mattioli et al. (2007) results, we believe that further analysis of the EII database is required to resolve these differences.

4.3. Updated CIE Calculations

The new recombination data of Badnell et al. (2003) and Badnell (2006a, 2006b, 2006c) motivated Bryans et al. (2006) to calculate new CIE fractional abundances. Their results show large differences from the Mazzotta et al. (1998) data for certain elements. Here we revise the work of Bryans et al. (2006) to include these newly recommended EII rate coefficients for all elements from H through Zn and some further updates to the DR and RR rate coefficients for selected ions.

We calculate CIE fractional abundances using the EII data of Dere (2007) for all ions of the elements H through Zn. We also include some corrections for Ca-like ions (K. P. Dere 2007, private communication). The DR and RR rate coefficients used here are those of Bryans et al. (2006) but updated to include recent corrections to the fitting of some of the rate coefficients (Badnell 2006b). We also include recent DR work for Mg-like ions of H through Zn and for Al- through Ar-like ions of Fe (Altun et al. 2007; Badnell 2006b, 2006d, 2006e). The DR and RR data for all other ions are those of Mazzotta et al. (1998).

Here we provide an electronic table of the CIE fractional abundances for all elements from H through Zn calculated using these data (Table 2; Fe shown only to illustrate the format and content). The tabulations are provided for a T_e range of 10^4–10^9 K. For ease of comparison with previous CIE fractional abundance calculations we present figures showing the present results along with those of Mazzotta et al. (1998) in Figure 1, and the present results along with those of Bryans et al. (2006) in Figure 2.

5. A NEW APPROACH TO DERIVE AVERAGE EMS AND TEMPERATURES

Using the method described in Section 3, the assumption of constant temperature and density, and our updated CIE results, we can calculate the EM curve for each of the observed spectral lines listed in Table 1. Due to oversimplifications of the plasma model, uncertainties in the observations, and errors in the atomic data, there is no common intersection of all EM curves at a single $[T_c, \mathrm{EM}_c]$. So one must calculate the most likely EM and T_e of the plasma based on the range of values where the EM curves cross one another. To determine these values we have developed a mathematically more rigorous approach than has been used in the past for isothermal plasmas. Here we use the emission lines from Si to illustrate this new method. We calculate the EM curves using a constant electron density of 1.8×10^8 cm^{-3} as was reported by Feldman et al. (1999) for the same source region.

Step 1 of our approach is to take the mean of all crossing points of the EM curves for a given group of lines. This can be seen in the left panel of Figure 3. In this panel we have marked with an asterisk every crossing point of the EM curves shown.

The EM versus T_e curves vary more slowly in log–log space than in linear space. Also, because of the shape of the curves, any outlying crossings are far more likely to occur at a higher EM than at a lower EM. Thus, those crossings that fall far from the preponderance skew the average always toward higher values of the EM. To avoid giving undue weight to these points we calculate the mean in log space, where $\langle \log_{10} \mathrm{EM} \rangle \leqslant \log_{10} \langle \mathrm{EM} \rangle$. This is equivalent to taking the geometric mean rather than the more common arithmetic mean.

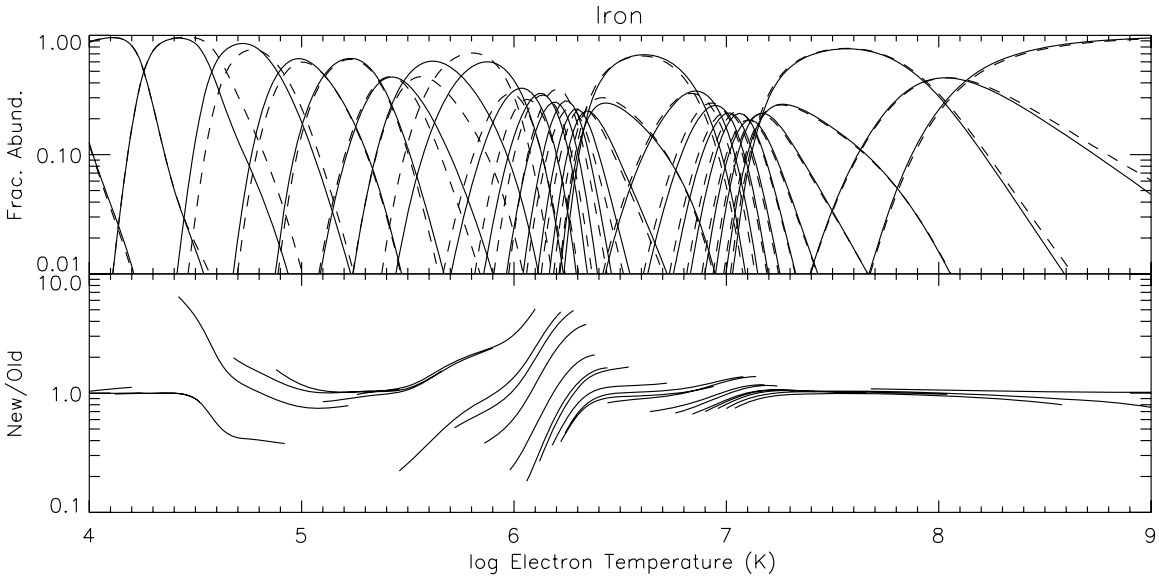

Figure 2. Ionization fractional abundance vs. T_e for all ionization stages of Fe. The upper graph shows our results (solid curves) and the abundances calculated by Bryans et al. (2006; dashed curves). The lower graph shows the ratio of the calculated abundances. Comparison is made only for fractional abundances greater than 10^{-2}. We label our results as "New" and those of Bryans et al. (2006) as "Old."

(An extended version of this figure set is available in the online journal.)

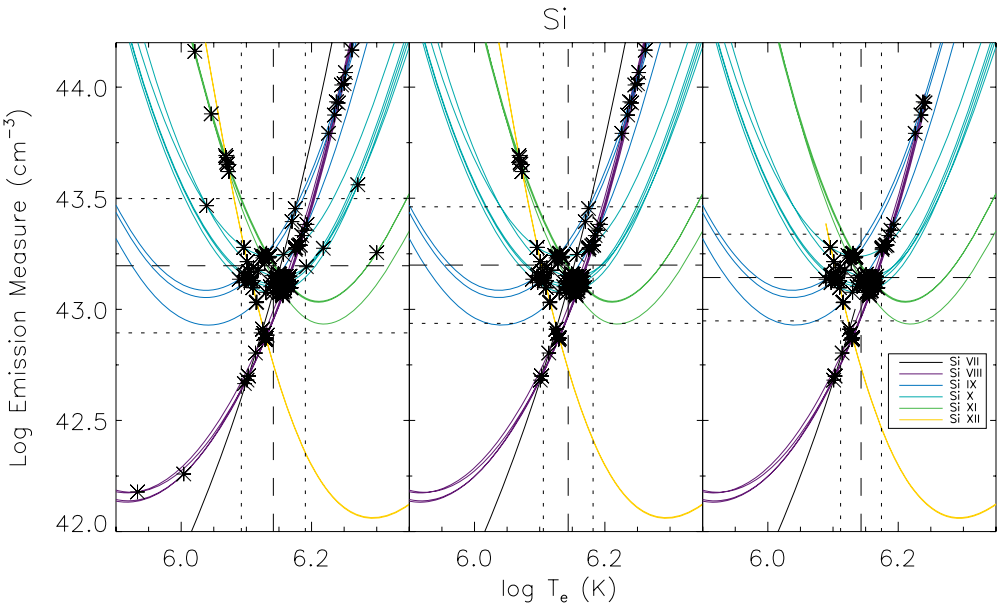

Figure 3. EM vs. T_e curves of all emission lines observed here from Si. The dashed lines indicate the mean $\log_{10}\mathrm{EM}$ and $\log_{10} T_e$ and the dotted lines show the standard deviations of these values. Asterisks indicate where the curves cross. The left panel shows the results after Step 1 of the analysis, the middle panel shows the results after Step 2, and the right panel shows the results after Step 3. See Section 5 for a description of each step.

The log of the geometric mean EM is given by

$$\langle \log_{10} \mathrm{EM} \rangle = \log_{10} \left(\prod_{i=1}^{n} \mathrm{EM}_i \right)^{1/n} = \frac{1}{n} \sum_{i=1}^{n} \log_{10} \mathrm{EM}_i \quad (7)$$

and its standard deviation by

$$\delta \langle \log_{10} \mathrm{EM} \rangle = \sqrt{\frac{\sum_{i=1}^{n} (\log_{10} \mathrm{EM}_i - \langle \log_{10} \mathrm{EM} \rangle)^2}{n}}, \quad (8)$$

where n is the number of crossing points over which the mean is being taken and EM_i is the value of EM at each of these crossings. By a similar argument the mean and standard deviation of T_e are calculated in the same way. From here on, unless otherwise stated, when we discuss the mean and standard deviation of the EM and T_e we are referring to the geometric mean and geometric standard deviation. In Figure 3 the mean $\log_{10}\mathrm{EM}$ and mean $\log_{10} T_e$ are shown as dashed lines and the standard deviations by dotted lines.

Step 2 eliminates the less physically probable crossings when two EM curves cross one another more than once. For any two curves we select only the crossing point that is closest, in the $\log \mathrm{EM}$–$\log T_e$ plane, to the mean calculated values of the EM and T_e from Step 1. In Step 2 we also exclude some additional unphysical crossing points. In all cases where there

Table 3
Inferred FIP Enhancement Factors and Coronal Abundances Used in the Analysis Here

Element	FIP[a] (eV)	Photospheric Abundance[b]	FIP Enhancement Factor		Resulting Coronal Abundance	
			Current CIE Results	Mazzotta et al. (1998) CIE Results	Current CIE Results	Mazzotta et al. (1998) CIE Results
N[c]	14.53	−4.08	1.00	1.00	−4.08	−4.08
O[c]	13.62	−3.17	1.00	1.00	−3.17	−3.17
Ne	21.56	−3.89	1.00	1.00	−3.89	−3.89
Na[d]	5.14	−5.67	$7.75^{+12.98}_{-4.97}$	$7.84^{+19.98}_{-6.40}$	$-4.78^{+0.42}_{-0.45}$	$-4.78^{+0.55}_{-0.73}$
Mg	7.65	−4.42	$2.78^{+2.28}_{-1.25}$	$2.91^{+0.14}_{-0.13}$	-3.98 ± 0.26	-3.96 ± 0.02
Al	5.99	−5.51	$3.58^{+1.72}_{-1.16}$	$4.51^{+1.57}_{-1.17}$	-4.96 ± 0.17	-4.86 ± 0.13
Si	8.15	−4.44	$4.94^{+2.90}_{-1.82}$	$5.18^{+3.41}_{-2.06}$	-3.75 ± 0.20	-3.73 ± 0.22
S	10.36	−4.67	$2.19^{+0.21}_{-0.19}$	$1.78^{+0.31}_{-0.33}$	-4.33 ± 0.04	-4.42 ± 0.09
Ar	15.76	−5.41	1.00	1.00	−5.41	−5.41
K[d]	4.34	−6.87	$1.75^{+0.44}_{-0.59}$	$3.84^{+2.99}_{-1.30}$	-6.63 ± 0.35	$-6.29^{+0.25}_{-0.18}$
Ca[d]	6.11	−5.65	$3.46^{+4.29}_{-1.93}$	$6.67^{+11.70}_{-4.25}$	$-5.11^{+0.18}_{-0.10}$	-4.83 ± 0.44
Fe	7.90	−4.50	$6.98^{+1.42}_{-1.17}$	$5.06^{+0.62}_{-0.55}$	-3.66 ± 0.08	-3.80 ± 0.05

Notes. We list here the elements used in the present analysis along with their FIP. Also listed for each element is the photospheric abundance, the enhancement factor used to account for the FIP-effect, and the resulting coronal abundance. Enhancement factors and resulting coronal abundances are given for results of the GEM method using the CIE fractional abundances of this paper and those of Mazzotta et al. (1998). All abundances are given as $\log[n(\mathrm{X})/n(\mathrm{H})]$ with $n(\mathrm{X})$ the abundance of element X and $n(\mathrm{H})$ the abundance of hydrogen.

[a] Dragoset et al. (2001).

[b] Feldman & Laming (2000).

[c] As discussed in Section 8.4, we believe N and O to be from a cooler plasma so we do not determine their EM by interpolation and assume a FIP factor of 1 in accordance with other high-FIP elements. See also Section 6 and Figure 6 for further details.

[d] Insufficient number of crossings to determine the mean EM so we calculate the FIP factor by using the EM at $\log_{10} T_e = 6.13 \pm 0.06$. See Section 6 and Figure 6 for further details.

are multiple emission lines from a single ion, the EM curves are nearly parallel. Often, these curves nearly overlap with one another and can cross in one or more places. We attribute the crossings of these lines to errors in the effective line emission rate coefficients and/or issues with the observed line intensities. For this reason, we exclude these crossings from our calculation. For Si emission lines, such crossings are seen for Si VIII, Si X, and Si XI (Figure 3). Using this reduced set of crossings we recalculate the mean and standard deviation of the EM and temperature. This plot is shown in the middle panel of Figure 3.

In Step 3 we further reduce the data set by considering only EM curves in the temperature range where $f^m \geqslant 0.01$. The reliability of all published CIE calculations is uncertain below this fractional abundance. Bryans et al. (2006) compared the results of CIE calculations using two different compilations of state-of-the-art DR and RR data sets. Agreement at peak abundance was found to be within 10% and within 50% when going to temperatures where the fractional abundance is 0.01. Outside this temperature range, for values of $f^m < 0.01$, the reliability of the CIE calculations grows significantly worse.

In the right panel of Figure 3 we show the same EM curves as in the middle panel but only for the temperature range where $f^m \geqslant 0.01$. It is this mean EM and T_e after Step 3 that we consider the most likely EM and T_e for a given set of emission lines. Henceforth, when discussing the results after all three steps of our analysis, we refer to the EM and T_e as coming from the Geometric mean EM (GEM) method.

6. CORONAL ABUNDANCE ENHANCEMENT FACTORS

Our first step in determining the coronal abundance of the observed elements is to assume that the high-FIP elements Ne and Ar have the same abundance in the corona as they do in the photosphere. This follows the approach taken by Feldman et al. (1998). Using the photospheric abundances of Feldman & Laming (2000; see Table 3), we have calculated the geometric mean EM from emission lines of Ne and Ar using the GEM method outlined in Section 5, giving $\langle \log_{10} \mathrm{EM}_{\mathrm{high-FIP}} \rangle$.

An objective of this paper is to investigate the apparent abundance discrepancy of Li- and Na-like ions. Previous studies, such as those of Dupree (1972), Feldman et al. (1998), and Landi et al. (2002), have found the abundance of these ions to be greater than those of ions in other isoelectronic sequences. In order that this discrepancy does not affect our calculation of the FIP factors of each element, we do not include any Li- or Na-like lines in the calculations of the FIP factors detailed below.

Landi et al. (2002) also reported a difference in T_e derived from N-like and non-N-like ions within Group I. However, unlike the Li- and Na-like abundance discrepancy, this has not been reported in the literature previously. If we adopt the uniform FIP factor of 3.5 used by Landi et al. (2002) for all high-FIP N-like and non-N-like ions and implement our GEM method we find no discrepancy in the T_e derived from N-like and non-N-like ions. This is discussed in more detail in Section 8. For these reasons, in this section we include both N-like and non-N-like ions in our analysis.

The results of the GEM analysis of the high-FIP elements can be seen in the upper-left panel of Figure 4. The exclusion of the Li- and Na-like ions results in only a single crossing remaining after the three steps—due to two emission lines from Ar XI and Ar XII. We use the value of the EM at this point as our reference value. Restricting the temperature range to that where the fractional abundance of an ion is greater than 1% limits us to this single crossing since the two Ne VII EM curves are below this limit at the T_e values where they cross the EM curves of Ar XI and Ar XII. It is not ideal that we are left with only a single crossing but we believe this represents an improvement

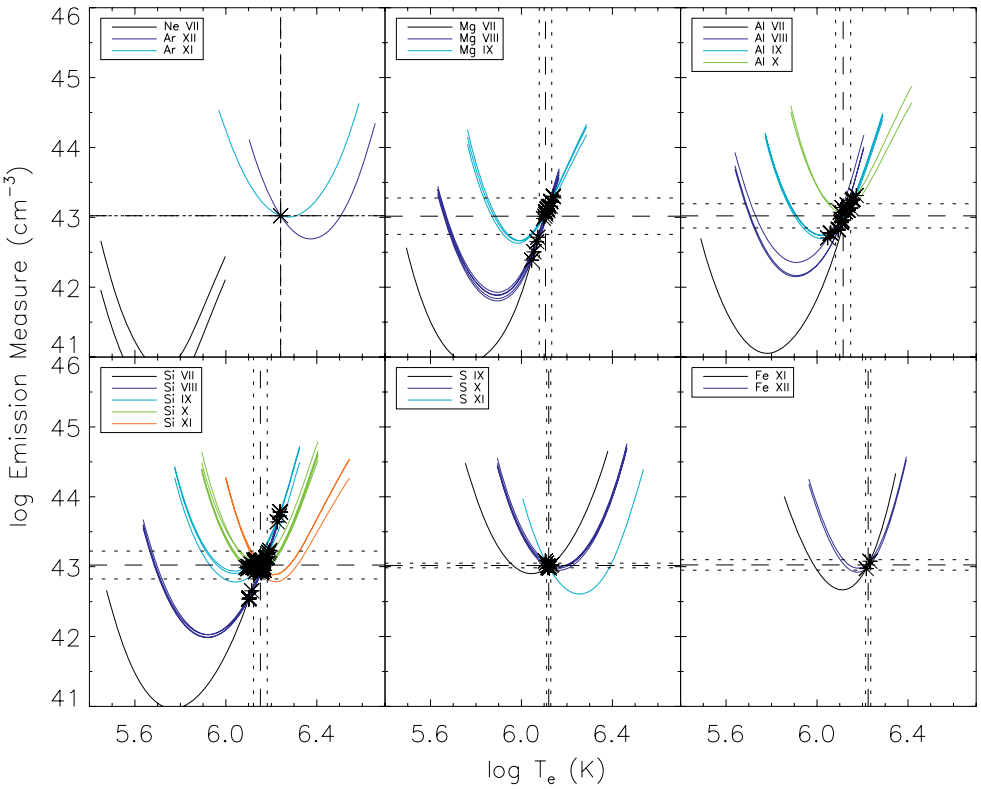

Figure 4. EM vs. T_e curves of all the emission lines from each of the low- and moderate-FIP elements using the GEM method described in Section 5. Na, K, and Ca are excluded as in this SUMER data set there are not enough observed emission lines from these elements to determine a mean EM. The upper left panel shows the high-FIP elements Ne and Ar.

over the work of Feldman et al. (1998). There they used only a single line, whereas here we use two. Additionally, the line they selected was Li-like O VI. As we have discussed above, and will also discuss in Section 8, there are several reasons to treat this line with suspicion. It is also worth noting that the crossing of the Ar lines results in $\log_{10} T_e = 6.24$. This is ~ 0.1 in the dex higher than the temperature derived from the other emission lines (see later in this section and Section 7). However, in the absence of additional non-Li- and Na-like emission from other high-FIP elements, we consider normalizing to this crossing of Ar lines to be the best approach to analyzing this particular observation.

We next separate all other emission lines by the element responsible for the emission and, again using the GEM method, calculate the mean EM of each of the low- and moderate-FIP elements individually using the photospheric elemental abundances as our starting value, giving $\langle \log_{10} \mathrm{EM_X} \rangle$ for each element X. For each of these low- to moderate-FIP elements, we determine an "enhancement factor" f_X for the elemental abundance that will result in the same derived EM as found for the high-FIP element Ar. From Equations (2) and (5) we see that the elemental abundance

$$f(X) = \frac{n(\mathrm{X})}{n(\mathrm{H})} \tag{9}$$

is inversely proportional to the EM of the emitting plasma, so the f_X values can be calculated as

$$\log_{10} f_\mathrm{X} = \langle \log_{10} \mathrm{EM_X} \rangle - \langle \log_{10} \mathrm{EM_{high-FIP}} \rangle, \tag{10}$$

where

$$f_\mathrm{X} = \frac{f(X)_\mathrm{corona}}{f(X)_\mathrm{photosphere}}. \tag{11}$$

For the emission from the elements Mg, Al, Si, S, and Fe, we show the EM as a function of T_e in Figure 4 where we have used our derived coronal elemental abundances. These are subject to the three steps of the GEM method but in this case we only show the last step. The derived elemental abundances are given in Table 3.

From Equation (10), we estimate the absolute error in $\log_{10} f_\mathrm{X}$ as the quadrature sum of the standard deviations of the EM from the high-FIP elements and the EM from the individual element X, i.e.,

$$\delta \langle \log_{10} f_\mathrm{X} \rangle = \sqrt{\delta \langle \log_{10} \mathrm{EM_X} \rangle^2 + \delta \langle \log_{10} \mathrm{EM_{high-FIP}} \rangle^2}\,. \tag{12}$$

However, since only a single crossing of Ar lines is used to determine the high-FIP EM, there is no error associated with $\log_{10} \mathrm{EM_{high-FIP}}$ and the error in $\log_{10} f_\mathrm{X}$ reduces to $\delta \langle \log_{10} \mathrm{EM_X} \rangle$ and is thus probably an underestimate. Given our derived errors in $\langle \log_{10} \mathrm{EM} \rangle$ presented in Section 7 we estimate $\langle \log_{10} \mathrm{EM_{high-FIP}} \rangle$ is good to $\sim \pm 0.3$ in the dex. However, due to insufficient data, we do not attempt to assign an error to $\delta \langle \log_{10} \mathrm{EM_{high-FIP}} \rangle$. Instead, we leave the errors in the FIP factors as they are, but note that they are likely underestimates.

With the Li- and Na-like lines omitted, we are left with only two emission lines from Na and Ca and a single emission line from K in this observation. Both Na emission lines are from the same charge state and their associated EM curves are therefore almost parallel. The same is true for the two emission lines from Ca. We thus have no crossing points of the EM curves over the T_e range considered for Na, K, and Ca. Also, as discussed in Section 8, we believe the emission from Li-like N V and O VI ions to be from a cooler region of plasma so we do not determine an average EM from the curves crossings of these elements.

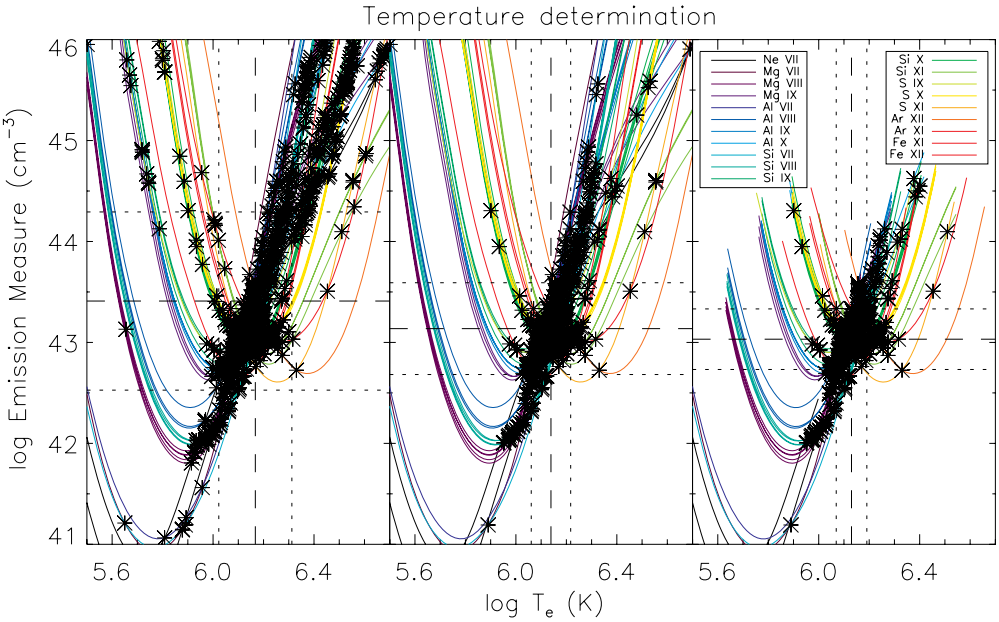

Figure 5. EM vs. T_e curves of all the emission lines from each of the elements Ne, Mg, Al, Si, S, Ar, and Fe (excluding Li- and Na-like ions). The T_e derived from these elements were used to determine the FIP factors of Na, K, and Ca. Asterisks indicate where the curves cross. The three panels show the three steps of the GEM method as in Figure 3.

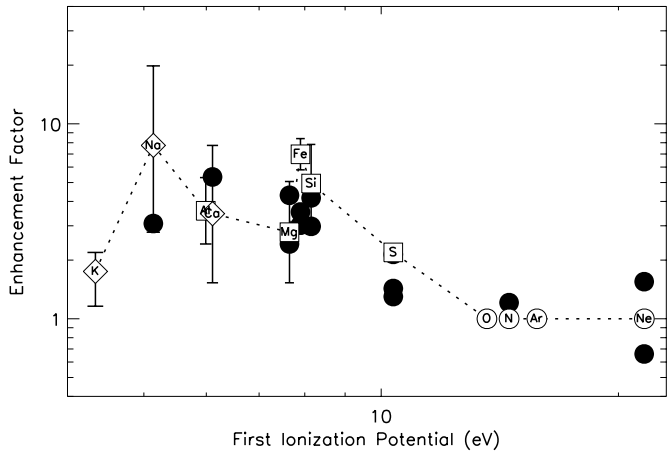

Figure 6. Coronal abundance enhancement factor (i.e., FIP factor) used for each of the elements vs. their FIP. Open circles indicate the high-FIP elements O, N, Ne, and Ar where no enhancement was assumed. The elements in squares indicate those which had their enhancement factor determined by matching their mean EM with that of the high-FIP element Ar. Elements marked with diamonds are those that did not have enough crossings to determine their EM in this way (see Section 6 for further details). The data points for Al and Ca overlap. The dotted line is purely to guide the eye. The solid circles are the results of Feldman et al. (1998) for N, O, Ne, Na, Mg, Si, S, Ca, and Fe. Feldman et al. (1998) scaled their results to O and assumed a FIP factor of 1 for this element. We also set the O FIP factor to 1, so their and our FIP factors for O lie directly on top of one another in this plot.

To determine the FIP factors of Na, K, and Ca, we use their EM values at the T_e determined from those emission lines for which we have already calculated FIP factors. This mean T_e determination is shown in Figure 5 where emission lines of Ne, Mg, Al, Si, S, Ar, and Fe have been considered (excluding Li- and Na-like ions). This gives a value of $\log_{10} T_e = 6.13 \pm 0.06$, at which value we calculate the EM of each of the Na, K, and Ca lines. (For Na and Ca, for which we have two emission lines, we take the average value of the two EM values at $\log_{10} T_e = 6.13$.)

We then determine a FIP factor for each of these elements that will give the same EM as for the high-FIP element Ar. We estimate the absolute error in $\log_{10} f_X$ of these three elements by calculating their EM at the values of the extremes of the errors associated with T_e, i.e., the EM at $\log_{10} T_e = 6.07$ and $\log_{10} T_e = 6.19$.

Table 3 lists the enhancement factors, which are often called FIP factors or FIP biases, for all of the elements present in the observation. We also give the resulting coronal elemental abundances. The FIP factors are also shown in Figure 6 alongside the results of Feldman et al. (1998). Note that Figures 3–6 show the results when using the CIE fractional abundances of this paper. We have repeated the analysis using the Mazzotta et al. (1998) CIE fractional abundances. We do not show figures of these results, but in Table 3 we list the FIP factors and coronal abundances determined when using these older CIE data.

7. ANALYSIS BY GROUPS

Using our derived coronal abundances we calculate the EM and T_e of each of the line categorizations given in Section 2. Figures 7–15 show the GEM approach as applied to each of these groups. We also give the results in Table 4 listing the geometric mean and standard deviation of the EM and T_e after each step of the GEM method.

For the Group I and II categorizations, we show their individual subcategorizations as well as the groups as a whole. In the case of Group IIb, the emission lines have been further subdivided by separating out the N V and O VI lines. This is because the EM curves from these lines do not match well with the others in this group. We elaborate on the possible reasons for this in Section 8. When we consider Group II as a whole, these lines are also excluded.

In addition to the division by groups we calculate the mean EM and T_e from every emission line (but again excluding the Li-like N V and O VI lines). This is done both including and

Table 4
Derived T_e and EM

Figure	Group	Step[a]	$\langle \log_{10} T_e \rangle$ (K)	$\delta\langle \log_{10} T_e \rangle$ (K)	$\langle \log_{10} \mathrm{EM} \rangle$ (cm^{-3})	$\delta\langle \log_{10} \mathrm{EM} \rangle$ (cm^{-3})
7	Ia	1	6.16	0.11	43.24	0.66
7	Ia	2	6.17	0.07	43.10	0.45
7	Ia	3	6.16	0.07	43.02	0.15
8	Ib	1	6.15	0.10	43.03	0.62
8	Ib	2	6.16	0.05	42.97	0.27
8	Ib	3	6.16	0.05	42.94	0.27
9	I	1	6.16	0.09	43.09	0.51
9	I	2	6.16	0.07	43.05	0.37
9	I	3	6.17	0.05	43.00	0.20
10	IIa	1	6.04	0.26	42.99	0.74
10	IIa	2	6.02	0.22	42.92	0.53
10	IIa	3	5.98	0.19	42.62	0.36
11	IIa*	1	6.13	0.20	42.97	0.56
11	IIa*	2	6.11	0.19	42.95	0.56
11	IIa*	3	6.06	0.12	42.73	0.30
12	IIa[b]	1	5.79	0.30	42.50	0.91
12	IIa[b]	2	5.84	0.27	42.70	0.84
12	IIa[b]	3	5.44	0.00	41.44	0.00
13	IIb	1	6.14	0.12	43.25	0.75
13	IIb	2	6.11	0.06	43.05	0.32
13	IIb	3	6.11	0.04	43.00	0.21
14	II	1	6.12	0.15	43.09	0.70
14	II	2	6.11	0.09	42.98	0.39
14	II	3	6.10	0.06	42.91	0.26
15	III	1	6.23	0.21	43.66	1.14
15	III	2	6.17	0.10	43.40	0.59
15	III	3	6.12	0.01	43.07	0.03
16	All Lines*	1	6.16	0.16	43.26	0.83
16	All Lines*	2	6.14	0.10	43.08	0.46
16	All Lines*	3	6.12	0.07	42.98	0.29
17	All Lines[c]	1	6.17	0.15	43.40	0.90
17	All Lines[c]	2	6.14	0.08	43.15	0.46
17	All Lines[c]	3	6.13	0.06	43.02	0.29

Notes. We list the geometric mean and standard deviation of the EM and T_e of each group categorization after each of the three steps outlined in Section 5. These results use the adjusted coronal elemental abundances as listed in Table 3.
* Excluding N V and O VI lines.
[a] As defined in Section 5.
[b] Only N V and O VI lines.
[c] Excluding all lines from Li- and Na-like ions.

excluding Li- and Na-like ions with the results shown in Figures 16 and 17, respectively, and listed in Table 4. It should be noted that this is not simply the sum of all the crossings from the individual groups. It also includes crossings between lines from different groups and results in a total of 1428 and 872 crossings (including and excluding Li- and Na-like lines, respectively).

The results of our analysis, as given in Table 4, are shown in graphical form in Figure 18 for the variation of $\log_{10}$ EM versus group, and Figure 19 for the variation of $\log_{10} T_e$ with group. The numbers in the data points in these figures are the number of crossings that were used to determine the average value and the errors shown are $\pm\delta\langle \log_{10} \mathrm{EM} \rangle$ of the mean. The average and standard deviation of $\log_{10}$ EM and $\log_{10} T_e$ as determined from every emission line are shown for comparison as dashed and dotted lines, respectively. We show these values with and without Li- and Na-like ions included in the EM calculation (i.e., Figures 16 and 17, respectively). The thick lines are the average and standard deviations when Li- and Na-like ions are included (excluding N V and O VI), and the thin are when they are excluded.

8. DISCUSSION

8.1. Updated CIE Fractional Abundances

One of the aims of this paper is to investigate the effect of our new CIE fractional abundances on the EM analysis. But first we look at how the updated recombination and ionization data impact the fractional abundances themselves. Perhaps the most widely used recommended CIE fractional abundances are those of Mazzotta et al. (1998). Comparison of the current CIE fractional abundances with these are shown in Figure 1. We also compare with the recently recommended CIE fractional abundances of Bryans et al. (2006) in Figure 2. A comparison of the works of Mazzotta et al. (1998) and Bryans et al. (2006) was discussed in Bryans et al. (2006), showing the effects of the new DR and RR data on the Mazzotta et al. (1998) results.

We compare the current CIE results with those of Mazzotta et al. (1998) for temperatures where $f^m \geqslant 0.01$. As discussed in Bryans et al. (2006) and in Section 5, the reliability of the atomic data is uncertain below this abundance. Differences between the current CIE results and those of Mazzotta et al. (1998) are large for all elements other than H, He, and Li. Factors of typically at least 2 difference in abundance are found for at least one ionization stage of each of these elements. Differences are often much larger. We draw particular attention to the extremely large differences in abundance and peak formation temperature of Sc, Ti, V, Cr, Mn, Co, Ni, Cu, and Zn in the T_e range of 10^4–10^6 K. Differences for these elements can be up to a factor of 30. Such variation between the current results and those of Mazzotta et al. (1998) is a result of the new recombination and ionization rate coefficients being used here.

We also compare our present results with the more recent recommended CIE fractional abundances of Bryans et al. (2006). The DR and RR rate coefficients used in this work are largely the same as those used by Bryans et al. with the exception of the Mg-like ions of H through Zn, the Al- through Ar-like ions of Fe, and some corrections to the fitting of other ions. The most significant changes in atomic data between this work and Bryans et al. (2006) is the introduction of the Dere (2007) EII rate coefficients. As expected, differences between the present results and those of Bryans et al. (2006) are not as large as those found between the present results and those of Mazzotta et al. (1998). However, large differences do remain. The differences highlighted above for Sc, Ti, V, Cr, Mn, Co, Ni, Cu, and Zn in the T_e range of 10^4–10^6 K are also present in the comparison with Bryans et al. For other elements, abundance differences of a factor a few are not uncommon. We attribute all these differences primarily to the EII rate coefficients.

In Sections 8.2 and 8.4 we discuss the impact of these updated CIE calculations on the analysis of the present SUMER observation. However, only a selection of the ions discussed in this section are present in the SUMER observation. We recommend that the CIE fractional abundances provided here be used in all future analysis of astrophysical spectra until the next revision of the CIE fractional abundances is published.

8.2. Comparison With FIP Factor Observations

For this same SUMER observation, FIP factors were also determined by Feldman et al. (1998). The present results are shown in comparison to those of Feldman et al. in Figure 6. They recommend a FIP factor of 1 for the high-FIP elements, a factor of 4 for the low-FIP elements, and a factor of somewhere

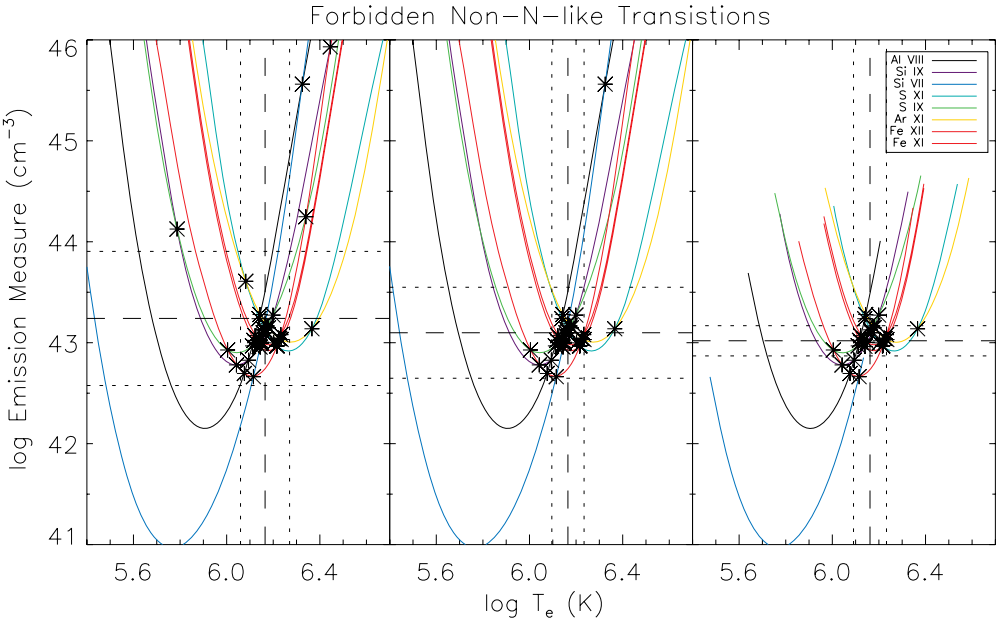

Figure 7. EM vs. T_e curves for the emission lines of Group Ia using our inferred coronal abundances. Asterisks indicate where the curves cross. The three panels show the three steps of the GEM method as in Figure 3.

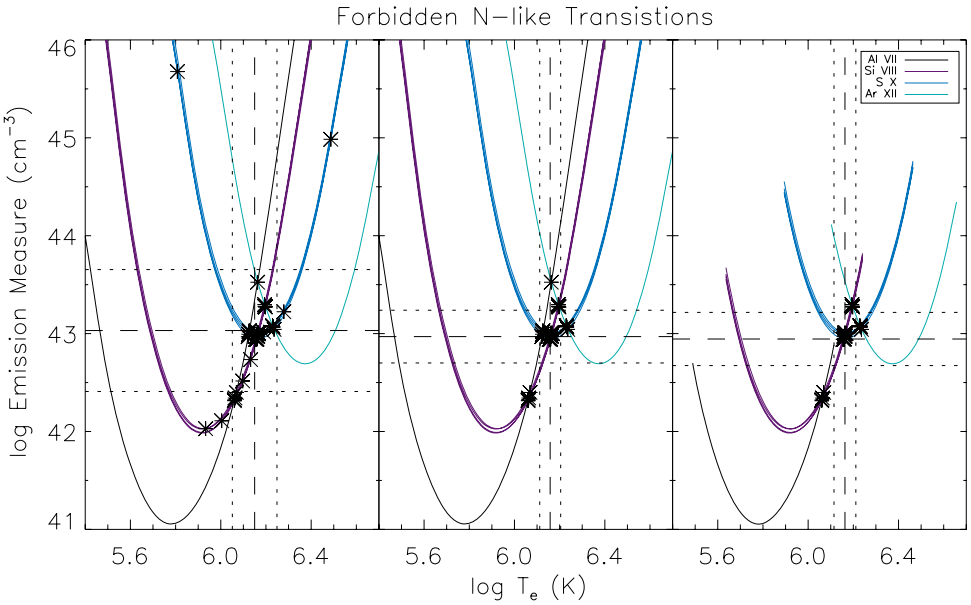

Figure 8. Same as Figure 7 but for Group Ib.

between 1 and 2 for S. These results are the basis of the approach taken by Landi et al. (2002) who assumed a FIP factor of unity for the moderate- and high-FIP elements, S, O, N, Ar, and Ne, and a uniform factor of 3.5 for all of the low-FIP elements, K, Na, Al, Ca, Mg, Fe, and Si.

We believe our present results are more robust than those of Feldman et al. (1998). First, our reference EM value is taken from the crossing of two Ar EM curves whereas Feldman et al. (1998) use the emission from a single Li-like O VI line as their reference value. This O VI line had an order of magnitude more counts than any other line in the data set used by Feldman et al. (1998) and thus seems a natural reference emission line. However, given the apparent systematic abundance discrepancy of Li-like ions (which the authors acknowledge), the O VI line may not be the most reliable to use as an EM reference value.

Furthermore, in determining the FIP factor for each element we generally use more emission lines than Feldman et al. (1998). For most elements we have multiple emission lines, ranging from three lines for Fe to as many as 18 for Si. The only exceptions are the elements K, Na, and Ca as have already been discussed in Section 6. For K we only have one emission line and for Na and Ca we have two. Feldman et al. (1998), however, use only one or two emission lines to determine the FIP factors for each of the elements they consider.

An additional source of unreliability in the Feldman et al. (1998) results lies in the method they use to estimate the plasma temperature. They use the crossing points of curves of FIP factors versus T_e from different elements. They estimate $\log_{10} T_e = 6.13$ (the same value at which we ultimately arrive) but only calculate these FIP factor versus T_e curves on a temperature grid of 0.1 in the log. From their figures

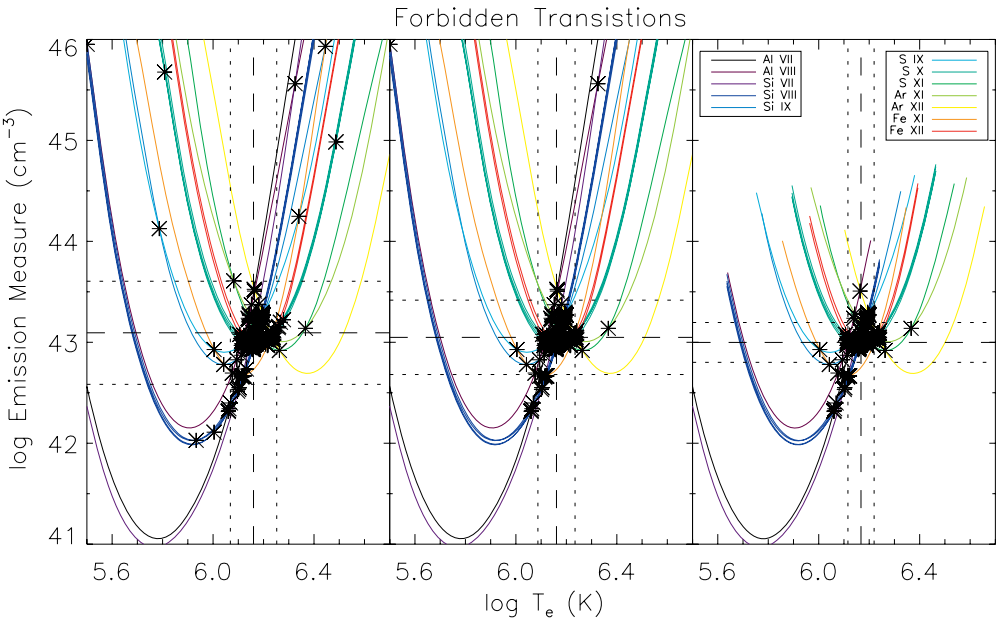

Figure 9. Same as Figure 7 but for Group I as a whole.

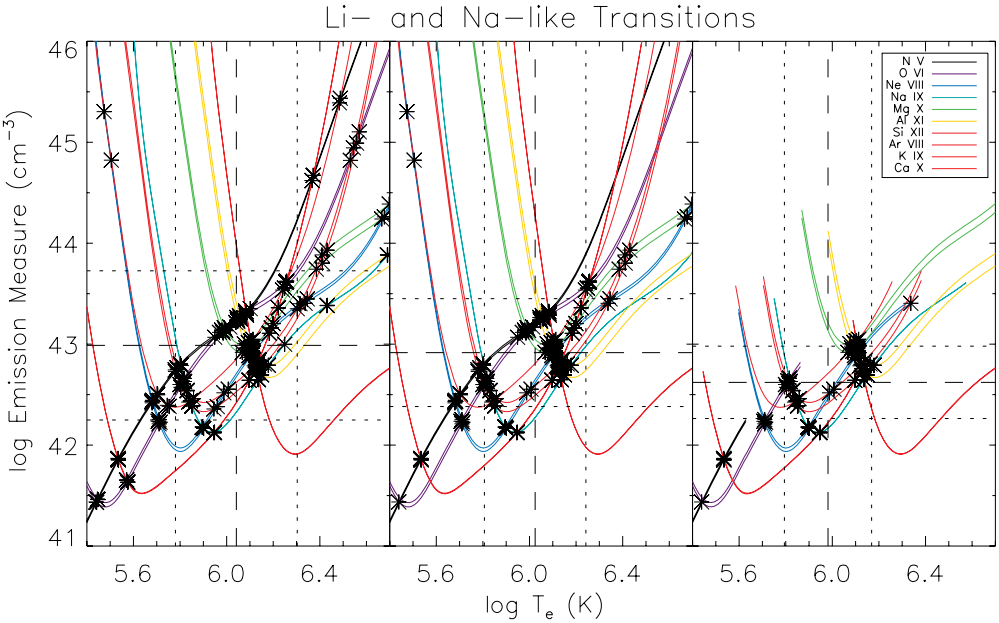

Figure 10. Same as Figure 7 but for Group IIa.

it is reasonable to conclude that any value in the range of $\log_{10} T_e = 6.1$ to 6.2 would fit their data points. In which case, their reported FIP factors could range from $\sim$ 1.5 to 11. However, Feldman & Laming (2000) estimate the error in these FIP factors to be of the order of 25% which seems to be a significant underestimate.

Of the low-FIP elements, we find rough agreement between our results and those of Feldman et al. (1998) in the sense that the abundance of the low-FIP elements is enhanced over the high-FIP elements, though one should note that Feldman et al. (1998) did not ascribe errors to their results. The largest differences between our results and those of Feldman et al. (1998) occur for Na and Ca, where we find differences of a factor of 2.5 and 1.5, respectively. However, our results for these elements should be considered with some care since they are not determined from an average of crossing points but from the EM at a given T_e. The error bars on our results for Na and Ca are also relatively large and the Feldman et al. (1998) results lie within these errors. Our result for K (a FIP factor of 1.75) is in disagreement with the Feldman et al. (1998) conclusion that the low-FIP elements are best fitted with an enhancement factor of 4. However, it should be noted that Feldman et al. (1998) did not calculate the FIP factor for K itself and that our analysis uses only one line of K.

Finally, we compare the FIP factor results of our GEM method when we utilize the CIE fractional abundances of this paper and those of Mazzotta et al. (1998). These results are given in Table 3. We find that the effect of our new CIE fractional abundances is largest for K, Ca, and Fe. In the case of K and Fe, the differences in the FIP factor are not within the estimated errors using our new CIE results. Naturally, these differences are also seen in the log of the inferred coronal abundances.

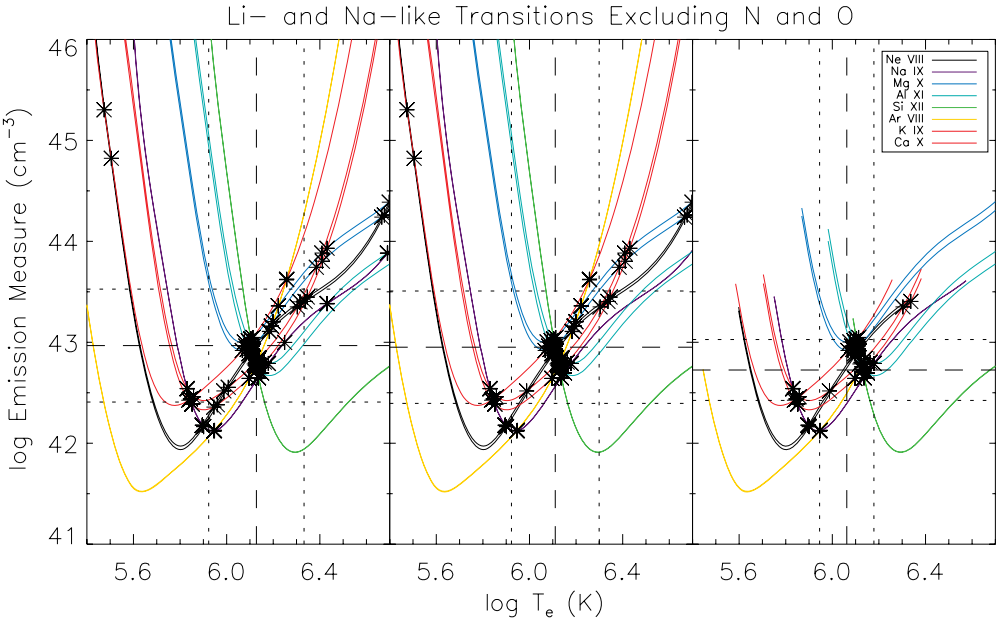

Figure 11. Same as Figure 10 but excluding emission lines from N v and O vi.

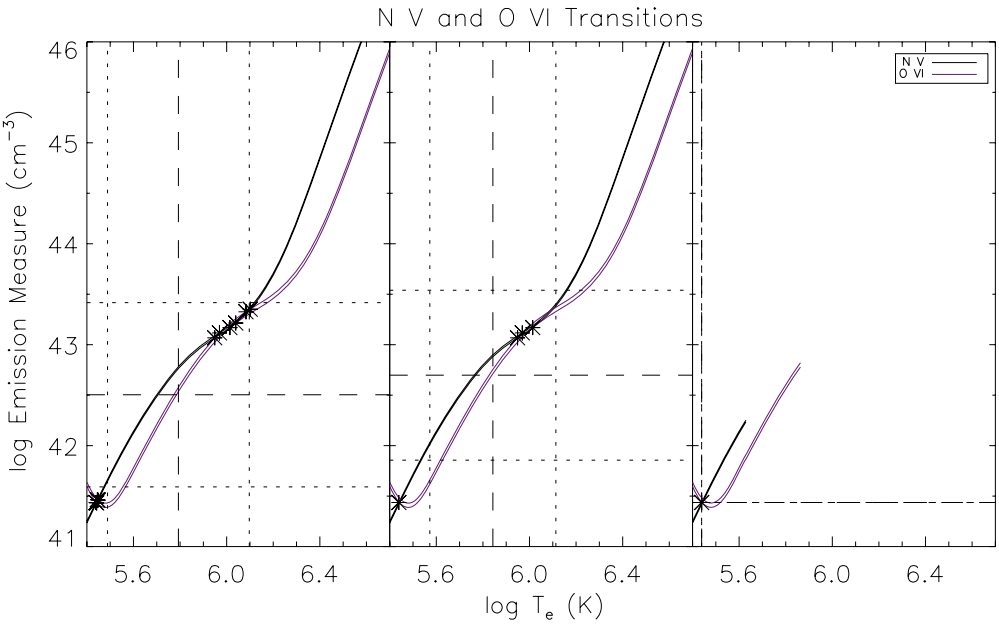

Figure 12. Same as Figure 10 but showing only emission lines from N v and O vi.

8.3. Comparison with the FIP Factor Model

The FIP effect model of Laming (2004, 2009) allows an opportunity to quantitatively compare our derived coronal elemental abundances with those of theory. The Laming model builds on that of Schwadron et al. (1999) by explaining the FIP effect in terms of Alfvén waves in the chromosphere. These Alfvén waves drive a pondermotive force on their reflection or transmission at the chromosphere–corona boundary which results in the elemental fractionation.

The extent of the FIP effect on each species is dependent on the upward energy flux of the Alfvén waves. Laming (2009) gives results for a number of wave energy fluxes and we compare these results with ours for wave energy fluxes of 2, 8, and 32 in units of 10^6 ergs cm^{-2} s^{-1}. We show these comparisons in Figure 20. Our results suggest that upward wave energy fluxes in this range best describe the solar conditions at the time of this particular SUMER observation. Our data generally fit the model well, with the exception of K. However, as has already been discussed in Section 6, our result for K should be considered less reliable than the other elements since we were limited to only a single K emission line in the SUMER observation.

It should also be noted that the low-FIP results of the present work were calculated relative to a high-FIP enhancement of 1, while in the Laming model the high-FIP elements do show a slight abundance variation dependent on their FIP value. If we were to normalize to the Ar FIP factor of the Laming (2009) model this would introduce a shift in our FIP factors of somewhere between a factor of 0.88 to 1.77.

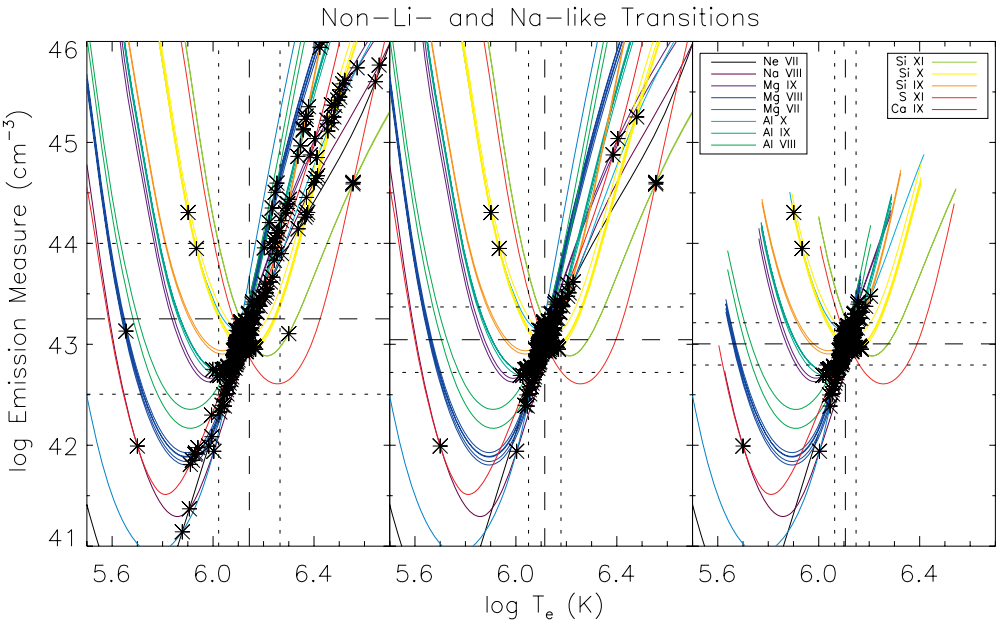

Figure 13. Same as Figure 7 but for Group IIb.

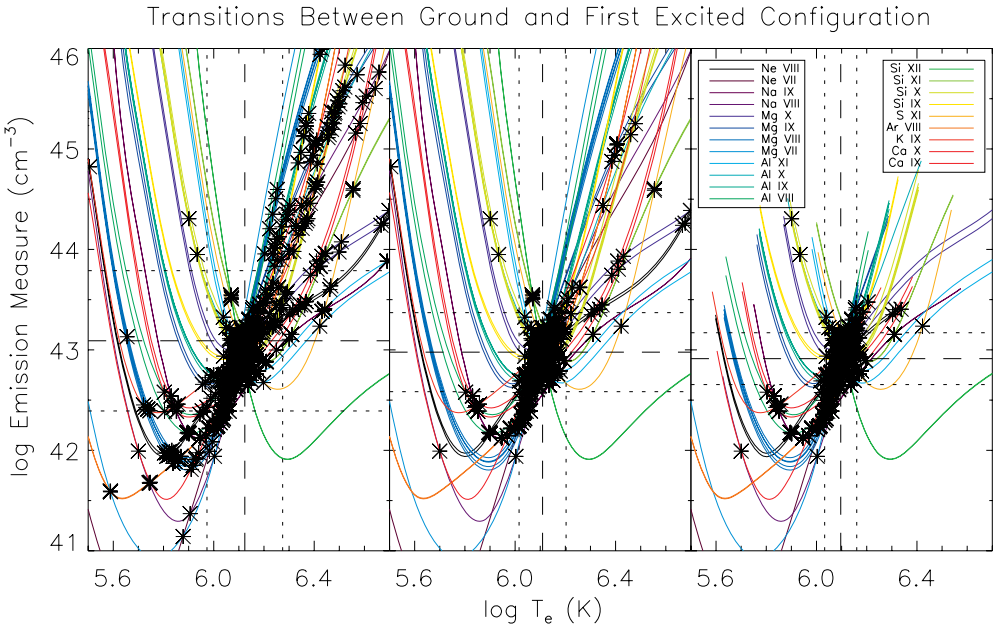

Figure 14. Same as Figure 7 but for Group II as a whole, excluding emission lines from N v and O vi.

8.4. Groups

We have used the same group splitting as that used by Landi et al. (2002) and thus can compare directly with their results. Table 5 shows their results for the mean and "error" of $\log_{10}$ EM and $\log_{10} T_e$ for the various groups. However, unlike the present work, Landi et al. quotes the mean and the error as judged by eye as opposed to our GEM method. As our results demonstrate, they have considerably underestimated the uncertainty of their results.

The results of Landi et al. (2002) suggest a difference in the temperature derived from the subsets of Group I, with $\log_{10} T_e = 6.13 \pm 0.01$ and 6.17 ± 0.01 for Groups Ia and Ib, respectively. We do not see this difference in our analysis. In the present work, Groups Ia and Ib give $\log_{10} T_e = 6.16 \pm 0.07$ and 6.16 ± 0.05, respectively. Within our error bars, we see no distinction between the N-like and non-N-like ions in this group. Using the same uniform low-FIP factor of 3.5 used by Landi et al. (2002) and the GEM method, the distinction remains unobserved as we find values of $\log_{10} T_e = 6.16 \pm 0.05$ and 6.17 ± 0.03 for Groups Ia and Ib, respectively. The temperatures derived from Groups IIa* (Henceforth, we use * to indicate that N v and O vi emission lines have been excluded from the calculation), IIb, and III agree reasonably well with those of Landi et al. (2002). We note that Landi et al. excluded the N v and O vi lines from their calculation of the Group IIa lines. When comparing with their results we also exclude these lines.

Figure 10 shows the EM curves for the lines in Group IIa. The largest discrepancies from the other lines in this group can be seen to come from the two pairs of N v and O vi lines. It is

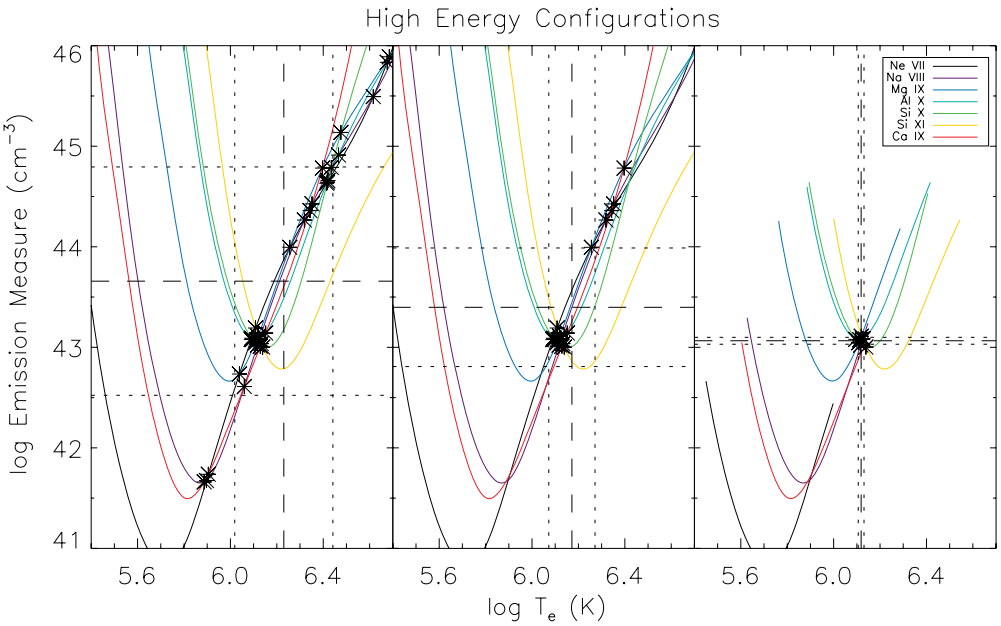

Figure 15. Same as Figure 7 but for Group III.

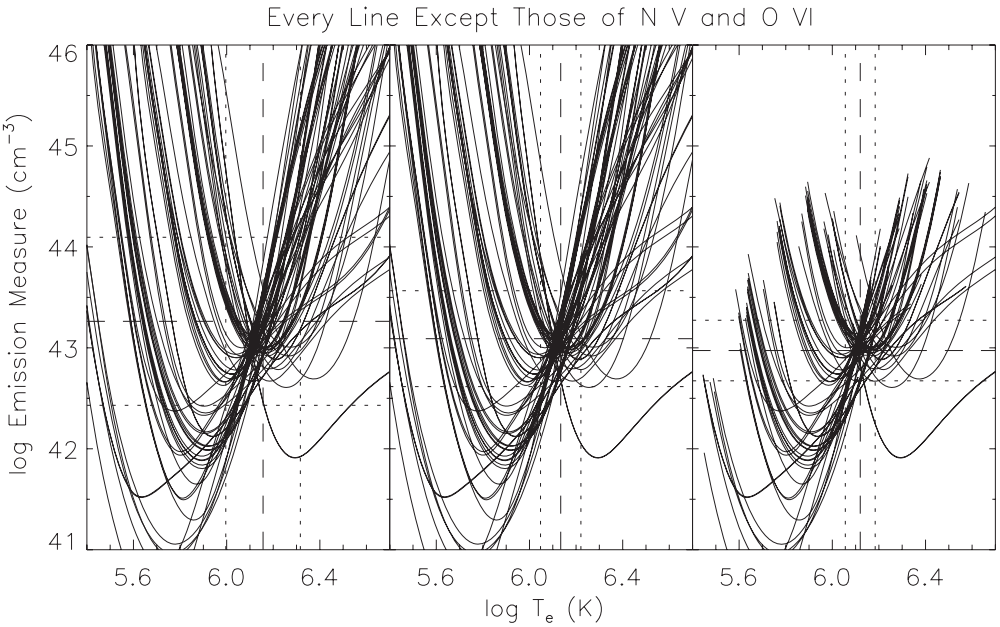

Figure 16. Same as Figure 7 but for all emission lines in the observation except those from N v and O vi. Due to the large number of crossings we exclude the asterisks for clarity.

interesting to note that these lines are the lowest in temperature of peak formation of all the ions considered here (see Figure 2 and Table 2), and as a result the majority of the crossings from these lines are excluded in the right panel of Figure 10 when we ignore fractional abundances below 0.01. This perhaps goes some way to highlight the need for care when using fractional abundances of such low values.

Given the disagreement with the other lines in Group IIa, and the lower formation temperature of N v and O vi compared to the other ions in the group, it is possible that the emission lines from these two ions originate from a different region of plasma. Thus, we have excluded the O vi and N v lines and recalculated the EM curves. Figure 11 shows this reduced set of EM curves. We have also done the same for the O and N lines on their own in Figure 12. A much lower average temperature of $\log_{10} T_e = 5.44$ is derived from these curves. We do not give an estimated error on this value since the final result comes from a single crossing point and has no standard deviation. Given that the N v and O vi ions have lower formation temperatures than the other ions of this observation, this suggests that the source of emission from these ions is from a different region of plasma with a lower temperature than that emitting the lines from other elements.

One of the questions that this paper seeks to address is the apparent discrepancy between the EMs derived from Li- and Na-like and that of all other ions. This has been identified previously (e.g., Dupree 1972; Feldman et al. 1998). All Li- and Na-like lines in this observation come from transitions between the ground and first excited configuration, i.e., our Group II. So we first investigate the difference between Li- and Na-like

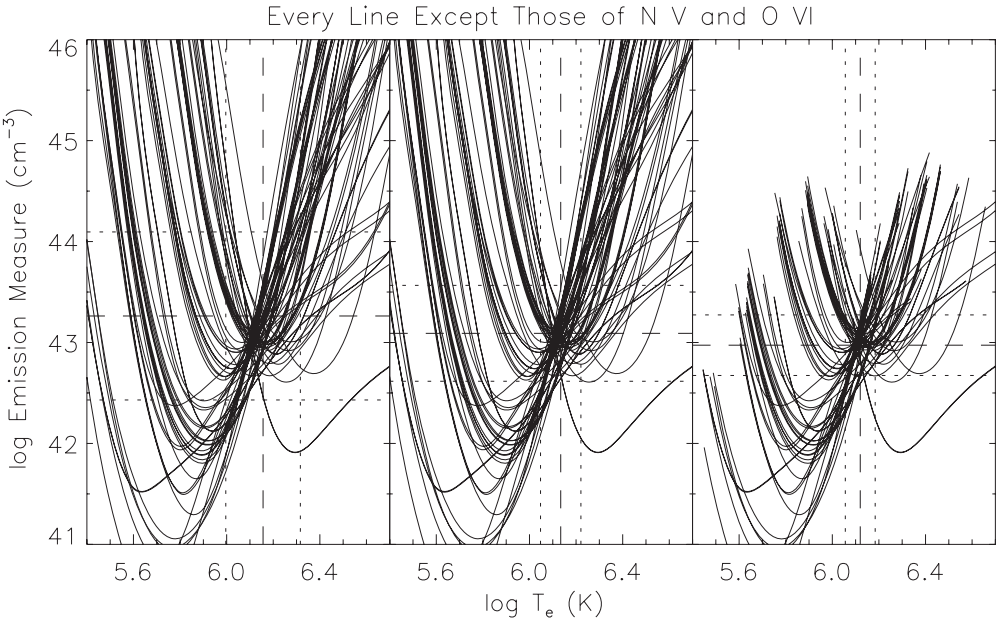

Figure 17. Same as Figure 16 but excluding emission lines from all Li- and Na-like ions.

ions and all other ions within this group. Our results for the Li- and Na-like ions are shown in Figure 11 (excluding N v and O vi) and can be compared to the EM from the other Group II ions shown in Figure 13. Results are also given in Table 4. A comparison of our present results and those of Landi et al. (2002) can be seen in Table 5. The combination of using the most up-to-date atomic data, an improved method of arriving at the most likely EM and T_e, and a re-analysis of the FIP factors, has led to us finding no sign of any discrepancy between the emission of Li- and Na-like ions and all the other Group II ions. In the present case, the difference between the EM from Groups IIa* (excluding N v and O vi lines) and IIb is within the error bars on the EM of Group IIa*.

In addition to the comparison of EM within Group II, we also compare the EM from the Li- and Na-like ions (Group IIa*) with the EM derived from every other ion in the observation (i.e., those from Groups I, IIb, and III). The comparison between the EMs from the Li- and Na-like ions and all other ions is shown in Figure 18. One can see that the EM from Li- and Na-like lines alone (point IIa*) overlaps, within the errors, with the average determined excluding Li- and Na-like ions (thin dashed line). Thus, we find no statistically meaningful difference in the EM derived from Li- and Na-like ions and that from every other ion in the observation.

Given that we find fairly good agreement in EM and T_e between each of the group categories, our best estimate of the EM and T_e of the emitting plasma is found by applying our analysis method to every emission line (excluding the discrepant N v and O vi lines). These results are shown in Figure 16 and give $\log_{10}\mathrm{EM} = 42.98 \pm 0.29$ and $\log_{10} T_e = 6.12 \pm 0.07$. If, in addition to excluding the N v and O vi lines, we also exclude the Li- and Na-like lines then the calculated values become $\log_{10}\mathrm{EM} = 43.02 \pm 0.29$ and $\log_{10} T_e = 6.13 \pm 0.06$ (see Figure 17). Landi et al. estimate $\log_{10}\mathrm{EM} = 43.20 \pm 0.15$ and $\log_{10} T_e = 6.13$ (no error given) for the plasma by combining results from Groups I and IIb. Our results agree, within our errors, with those of Landi et al. (2002). Our results have larger errors, which we believe to be more realistic due to our more rigorous method of calculating the mean and standard deviation of EM and T_e.

Table 5
T_e and EM Values Derived Using the GEM Method and Our Current CIE Fractional Abundances, as well as Using the GEM Method with the Mazzotta et al. (1998) CIE Fractional Abundances[a]

Figure	Group	$\langle\log_{10} T_e\rangle$ (K)			$\langle\log_{10}\mathrm{EM}\rangle$ (cm^{-3})		
		Current CIE Results	Mazzotta et al. (1998) CIE Results	Landi et al. (2002)	Current CIE Results	Mazzotta et al. (1998) CIE Results	Landi et al. (2002)
7	Ia	6.16 ± 0.07	6.13 ± 0.06	6.13 ± 0.01	43.02 ± 0.15	43.09 ± 0.13	43.15 ± 0.10
8	Ib	6.16 ± 0.05	6.17 ± 0.03	6.17 ± 0.01	42.94 ± 0.27	42.92 ± 0.16	43.15 ± 0.05
11	IIa*	6.06 ± 0.12	6.03 ± 0.12	6.11 ± 0.02	42.73 ± 0.30	42.63 ± 0.26	42.90 ± 0.15
13	IIb	6.11 ± 0.04	6.10 ± 0.04	6.13 ± 0.01	43.00 ± 0.21	42.99 ± 0.22	43.30 ± 0.15
15	III	6.12 ± 0.01	6.11 ± 0.01	6.13 ± 0.01	43.07 ± 0.03	43.05 ± 0.04	43.45 ± 0.10

Notes. Here we list the mean values and errors of the $\log_{10}\mathrm{EM}$ and $\log_{10} T_e$ derived from the GEM method using the CIE fractional abundances of the current paper and of Mazzotta et al. (1998). We also list the results reported by Landi et al. (2002). These are grouped in the same way as Table 4 but the values of the mean and standard deviation were determined in Landi et al. (2002) by eye, rather than using the more rigorous method developed and implemented here.

* Excluding N v and O vi lines.

[a] We compare with the results given in Landi et al. (2002).

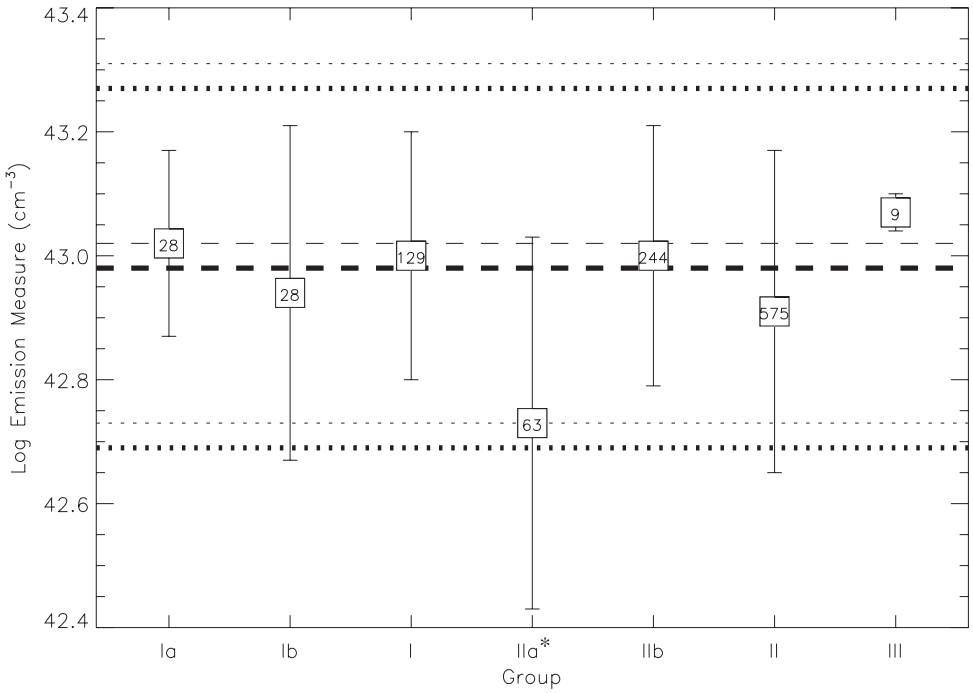

Figure 18. Mean $\log_{10}$ EM values for each of the groups using the GEM method (as listed in Table 4). The numbers in the data points represent the number of EM curve crossings that were used to derive the mean EM. The error bars on the points are $\pm\delta\langle\log_{10}\mathrm{EM}\rangle$. Group IIa* excludes the O VI and N V lines. The dashed and dotted lines indicate the mean and standard deviation, respectively, when every emission line, except N V and O VI, is considered. The thick lines include emission lines from Li- and Na-like ions (Figure 16) and the thin lines exclude emission lines from these ions (Figure 17).

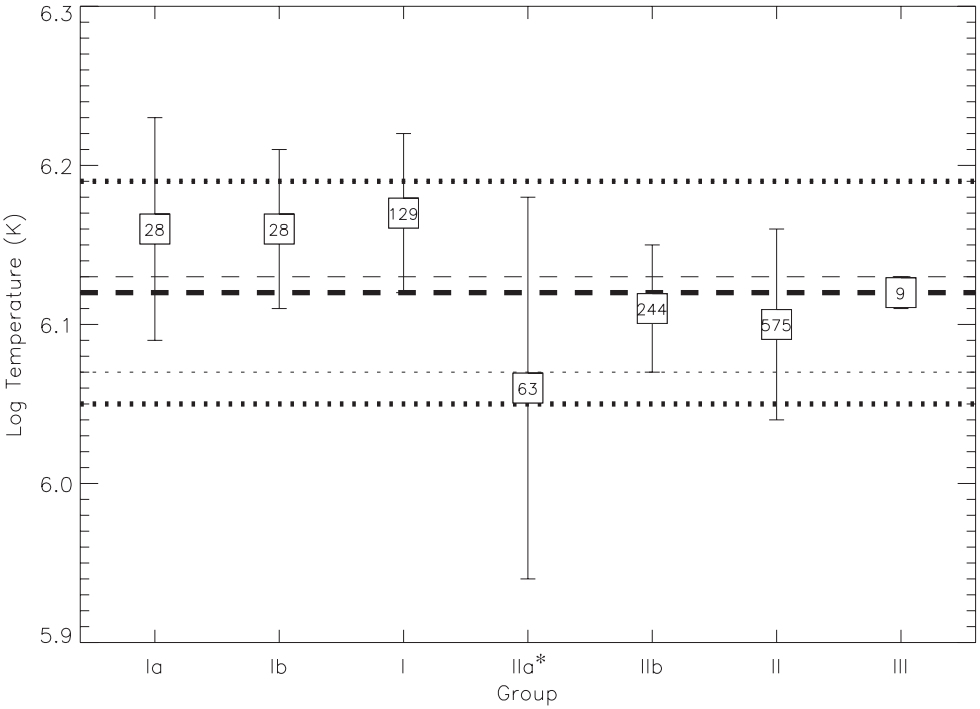

Figure 19. Same as Figure 18 but for $\log_{10} T_e$. The upper values of the standard deviation for the thick and thin lines lie on top of one another.

To investigate the effects of the updated CIE data on these results, we compare the EM and T_e derived for each group when utilizing the recommended CIE fractional abundances of this paper and those of Mazzotta et al. (1998). These results are given in Table 5. While differences are found, they are all within the errors. It is interesting to note that the large differences found in the FIP factors do not translate into differences on the same scale for the derived EM and T_e. Nonetheless, this would not necessarily be the case when applied to other observations, so we recommend the future use of the CIE fractional abundances presented here.

8.5. Other Issues

Despite an overall general agreement in the EM and T_e of each of the groups, there are a number of indications that the observed emission does not come from an isothermal plasma. We have already discussed the possibility that the Li-like N V and O VI lines come from a cooler region of gas. Even when these lines

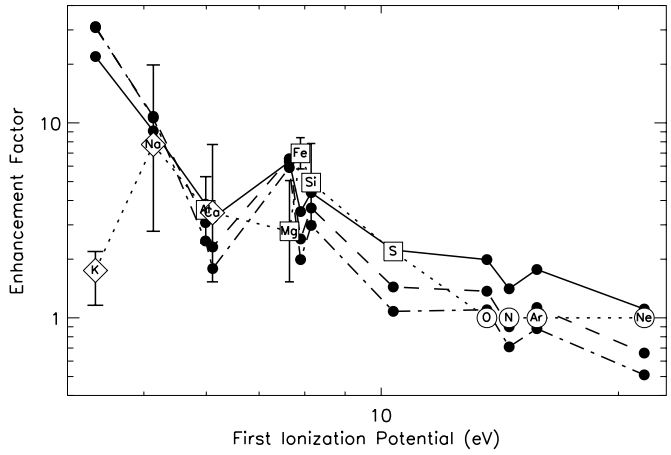

Figure 20. Coronal abundance enhancement factor (i.e., FIP factor) used for each of the elements vs. their FIP. Open symbols represent the present results; refer to Figure 6 for details. The data points for Al and Ca overlap. The solid circles are the results of the model of Laming (2009) for upward Alfvén wave energy fluxes of 2, 8, and 32 (solid, dashed, and dot-dashed lines, respectively) in units of 10^6 ergs cm^{-2} s^{-1}. Lines have been drawn between points only to guide the eye.

are removed from the Group IIa categorization, there remains a large scatter in the crossing points of the emission from Li- and Na-like ions (Figure 11) suggesting the isothermal assumption is not entirely accurate. There is also some evidence of a low-temperature component from Groups I and IIb (Figures 9 and 13, respectively). It is also possible that the relatively large errors in EM and T_e are suggestive of a non-isothermal plasma. To determine whether the crossings that fall away from the average are indeed a product of the non-isothermal nature of the plasma, and not some error in the atomic data, one would have to perform a differential EM (DEM) analysis, which is beyond the scope of this paper.

A further possible source of error in our analysis is that the ionization balance was calculated using the zero-density approximation. This issue has been raised by Feldman & Laming (2000) in reference to Fe^{8+} emission. They claim that over half of the population can be in metastable levels at coronal densities, but there are no emission lines from Fe^{8+} in the observation analyzed in this paper. The sensitivity of emission from Li-like ions has been investigated by Doyle et al. (2005). These authors found that the contribution function of emission from Li-like lines only becomes significantly affected on reaching densities $\geqslant 10^{11}$ cm^{-3}, orders of magnitude higher than the density of 1.8×10^8 cm^{-3} inferred by Feldman et al. (1999) for the observation analyzed here. We thus expect the zero-density approximation to be valid in this case, but a full density-dependent analysis of every emission line in the observation would be required before one could answer this issue with complete certainty. Again, such a study is beyond the scope of this paper.

9. PROPOSALS FOR FUTURE OBSERVATIONS

Our work shows that SUMER observations can go a long way toward constraining FIP models such as those of Laming (2004, 2009). Even better constraints can be achieved through the simultaneous observation of lines from a number of additional charge states. More lines from high-FIP elements such as N, O, Ne, and Ar are required to better determine the EM for these high-FIP elements, which can then be used to normalize the low-FIP elements. For N, O, and Ne, emission lines from H- and He-like stages need to be observed to avoid using Li-like ions. These charge states are predicted to be abundant for these elements at coronal temperatures. This may require simultaneous observations using separate, cross-calibrated spectrometers. For Ar, emission lines from the Ne-, F-, O-, and N-like ions would lie in the $6.0 \leqslant \log T_e \leqslant 6.2$ range typical of the corona. Additional line observations from elements such as Na, K, and Ca, for which we have few lines in the present observation, are also needed to better constrain their FIP factors.

10. SUMMARY

This work has re-analyzed data from a SUMER coronal observation in an attempt to improve upon previous methods of analysis. We have given a brief review of and implemented state-of-the-art electron–ion recombination and ionization data. We have updated the CIE results of Bryans et al. (2006) by using recently published DR data for Mg-like ions of the elements from H through Zn and for Al- through Ar-like Fe ions, and have updated the EII data to those of Dere (2007) for all ions of H through Zn. We have also set out a new, mathematically rigorous, approach for determining the EM and T_e of an emitting plasma within the isothermal approximation. Using these new CIE data and our approach for determining the EM, we calculated the FIP factors of the observed elements.

Our assessment is generally in reasonable agreement with a previous study of the FIP factors (Feldman et al. 1998). Also, we are in reasonable agreement with the FIP-effect model of Laming (2009) using an Alfvén wave energy flux in the range $\sim$ (2–32) $\times$ 10^6 erg cm^{-2} s^{-1}. However, our results differ from those of Landi et al. (2002) in certain respects. The difference between the temperature derived using lines from non-N- and N-like ions is not evident when we apply out analysis technique. Also, the previously reported discrepancy between the EM derived from Li- and Na-like lines and the EM from all other lines (Groups I, IIb, and III) is not supported by our results, rather the two agree at the 1σ level.

Our best estimate of the EM and T_e of the emitting plasma of this observation is $\log_{10}$ EM $= 42.98 \pm 0.29$ and $\log_{10} T_e = 6.12 \pm 0.07$ when we include all lines except those from N V and O VI, and $\log_{10}$ EM $= 43.02 \pm 0.29$ and $\log_{10} T_e = 6.13 \pm 0.06$ when we additionally exclude all Li- and Na-like lines. There remains variation in the crossing points of the EM versus T_e curves that are suggestive of errors in the atomic data, the observations, or the solar physics model used. However, from the results of the present work it is not possible to say where the source of these errors lie. Further improvements to the atomic database and new insight into the physical conditions of the upper solar atmosphere are needed before these questions can be answered. Given the evidence for regions of differing temperature, a DEM analysis might go some way to resolving the discrepancies found in this paper.

We thank H. Bruhns, H. Kreckel, J. M. Laming, and M. Lestinsky for stimulating discussions. We also thank K. P. Dere for providing corrected versions of his EII rate coefficients and for discussions thereon. CHIANTI is a collaborative project involving the NRL (USA), RAL (UK), MSSL (UK), the Universities of Florence (Italy) and Cambridge (UK), and George Mason University (USA). P.B. and D.W.S. were supported in part by the NASA Solar and Heliospheric Physics Supporting Research and Technology program and the NASA Astronomy and Physics

Research and Analysis Program. E.L. was supported by NASA grants NNG06EA14I and NNH06CD24 as well as other NASA grants.

REFERENCES

Altun, Z., Yumak, A., Yavuz, I., Badnell, N. R., Loch, S. D., & Pindzola, M. S. 2007, A&A, 474, 1051
Arnaud, M., & Rothenflug, R. 1985, A&AS, 60, 425
Aschwanden, M. J. 2004, Physics of the Solar Corona (Chichester: Praxis)
Badnell, N. R. 2006a, ApJS, 167, 334
Badnell, N. R. 2006b, http://amdpp.phys.strath.ac.uk/tamoc/DR/
Badnell, N. R. 2006c, http://amdpp.phys.strath.ac.uk/tamoc/RR/
Badnell, N. R. 2006d, J. Phys. B: At. Mol. Opt. Phys., 39, 4825
Badnell, N. R. 2006e, ApJ, 651, L73
Badnell, N. R., et al. 2003, A&A, 406, 1151
Bryans, P., Badnell, N. R., Gorczyca, T. W., Laming, J. M., Witthumsiri, W., & Savin, D. W. 2006, ApJS, 167, 343
Dere, K. P. 2007, A&A, 466, 771
Dere, K. P., Landi, E., Del Zanna, G., & Young, P. R. 2001, A&AS, 134, 331
Dere, K. P., Landi, E., Mason, H. E., Monsignori Fossi, B. C., & Young, P. R. 1997, A&AS, 125, 149
Doyle, J. G., Summers, H. P., & Bryans, P. 2005, A&A, 430, L29
Dragoset, R. A., Musgrove, A., Clark, C. W., & Martin, W. C. 2001, http://physics.nist.gov/PhysRefData/PerTable/index.html
Dupree, A. K. 1972, ApJ, 178, 527
Feldman, U., Doschek, G. A., Schühle, U., & Wilhelm, K. 1999, ApJ, 518, 500
Feldman, U., & Laming, J. M. 2000, Phys. Scr., 61, 222
Feldman, U., Schühle, U., Widing, K. G., & Laming, J. M. 1998, ApJ, 505, 999
Forbes, T. G. 2000, Phil. Trans. R. Soc. A, 358, 711
Foukal, P. V. 2004, Solar Astrophysics (2nd revised ed.; Weinheim: Wiley)
Gu, M. F. 2003a, ApJ, 589, 1085
Gu, M. F. 2003b, ApJ, 590, 1131
Gu, M. F. 2004, ApJ, 153, 389
Gudiksen, B. V., & Nordlund, Å 2005, ApJ, 618, 1020
Hundhausen, A. J. 1993, J. Geophys. Res., 98, 13177
Kingdon, J. B., & Ferland, G. J. 1996, ApJS, 106, 205
Klimchuk, J. A. 2006, Sol. Phys., 234, 41
Laming, J. M. 2004, ApJ, 614, 1063
Laming, J. M. 2009, ApJ, in press, arXiv:0901.3550
Landi, E., Feldman, U., & Dere, K. P. 2002, ApJS, 139, 281
Landi, E., et al. 2006, ApJS, 162, 261
Lang, J., Mason, H. E., & McWhirter, R. W. P. 1990, Sol. Phys., 129, 31
Mandrini, C. H., Démoulin, P., & Klimchuk, J. A. 2000, ApJ, 530, 999
Mattioli, M., et al. 2007, J. Phys. B, 40, 3569
Mazzotta, P., Mazzitelli, G., Colafrancesco, S., & Vittorio, N. 1998, A&AS, 133, 403
Priest, E. R., & Forbes, T. G. 2002, A&A Rev., 10, 313
Raymond, J., & Doyle, J. G. 1981, ApJ, 247, 686
Schwadron, N. A., Fisk, L. A., & Zurbuchen, T. H. 1999, ApJ, 521, 859
Summers, H. P., et al. 2006, Plasma Phys. Control. Fusion, 48, 263
Suno, H., & Kato, T. 2006, ADNDT, 92, 407
Tandberg-Hanssen, E., & Emslie, A. G. 1988, The Physics of Solar Flares (Cambridge: Cambridge Univ. Press)
Wilhelm, K., et al. 1995, Sol. Phys., 170, 75